LAWRENCE
LIVERMORE
NATIONAL
LABORATORY

LLNL-JRNL-858650

Simulation of Multiphase Flow and Poromechanical Effects around Injection Wells in CO2 Storage Sites

J. Huang, F. Hamon, M. Cusini, T. Gazzola, R. R. Settgast, J. A. White, H. Gross

December 21, 2023

Rock Mechanics and Rock Engineering

Disclaimer

Simulation of Multiphase Flow and Poromechanical Effects around Injection Wells in CO_2 Storage Sites

Jian Huang[1*], François Hamon[1], Matteo Cusini[2], Thomas Gazzola[1], Randolph R. Settgast[2], Joshua A. White[2], Herve Gross[1]

[1]*TotalEnergies E&P Research & Technology, Houston, TX 77002, U.S.A.*

[2]*Lawrence Livermore National Laboratory, Livermore, CA 94550, U.S.A.*

[*]*Corresponding author. E-mail address: jian.huang@totalenergies.com*

Highlights

- We introduce a fully coupled finite element/finite volume approach to simulate multiphase fluid flow and the associated rock deformations.
- This approach highlights how the coupling between rock deformations and multiphase fluid flow impacts short-term mechanical responses in the vicinity of the injection wells.
- The results of this numerical model are successfully verified against reference analytical solutions for multiphase flow and wellbore problems.
- We have tested the approach using both poroelastic and poroplastic deformations on an engineering problem, demonstrating the important effects of plasticity in CO_2 injection scenario.
- This work contributes to better operational decisions for designing CO_2 injection operations by assessing the containment potential of a site, and by analyzing the wellbore integrity during and after CO_2 injection.

Abstract In geological CO_2 storage operations, wellbore deformations and leakage pathways formations can occur around injection and abandoned wells subjected to high rates and long-term CO_2 injection. To guide engineering design and prevent CO_2 leakage risks, a full understanding of the underlying physics and robust numerical models are necessary to evaluate the response of underground formations in the near wellbore region and in the reservoir. In this study, a multi-scale and multi-physics open-source simulator (GEOS) is used to simulate multiphase flow and poromechanical deformations over time in three dimensions. The governing equations for mechanical deformations of the rock body and multiphase compositional fluid flow within the rock matrix are solved with a fully coupled finite element and finite volume approach. The Drucker-Prager model with friction hardening is applied to simulate elastoplastic deformation and a multiphase fluid model with power-law correlations for relative permeability is used to model the migration of CO_2 plume, which are coupled with numerical implicit scheme. Simulation results are verified against multiple analytical solutions for multiphase flow and wellbore problems, thus demonstrating the accuracy of this advanced simulator. In two engineering applications, we highlight the impact of elastoplastic deformation and coupled modeling for assessing induced displacements and stress perturbations, which are more pronounced in the near wellbore regions. This work focuses on short-term processes in the vicinity of injection wells where stress evolutions, rock deformations and multiphase compositional flow and transport are simulated jointly to ensure wellbore stability and prevent damage. This fully coupled geomechanical model can simulate multiphase flow and any associated poromechanical effects within the CO_2 storage site and in the surrounding formations. Such a large-scale, long-term, multi-physics simulation model is useful in many ways: it can guide operational decisions for CO_2 injection, assess the containment potential and risks of a site, and analyze the wellbore stability and integrity during and after CO_2 injection.

Keywords multiphase flow, poromechanics, implicit coupling, near wellbore, plasticity

1. INTRODUCTION

Geological carbon sequestration is a method to reduce atmospheric carbon dioxide concentrations by storing CO_2 in geological underground formations. The geomechanical deformations near CO_2 injectors can lead to operational and geological hazards. With high rates and long-term injections, leakage pathways can form around abandoned wells and

faults (Nogues et al., 2011; Gan et al., 2021). During and after CO_2 storage operations, it is important to preserve the wellbore and caprock integrity and mitigate CO_2 leakage risks (Bachu and Bennion, 2009; Vilarrasa, 2014; Torsæter et al., 2017; Onishi et al., 2019; Joulin et al., 2022).

Geomechanical deformations are due to pressure changes during injections in the pore space. The coupling between rock mechanical deformations and fluid flow and transport has been investigated in the literature (Rajapakse, 1993; Cappa and Rutqvist, 2011; Shi and Durucan, 2019). Terzaghi (1923; 1925) proposed the first linear poroelastic theory for solving one-dimensional soil consolidation problems under hydro-mechanical coupling. This theory was extended by Biot (1935; 1941) to describe soil consolidation in three dimensions. Their theory was developed for soft formations where the compressibility of solid grains and pore fluids is negligible. To generalize the poroelastic theory for deep geological formations, the deformations of matrix materials and pore fluids were included. Rice and Cleary (1976) reformulated the equations of poroelasticity with a distinction between drained and undrained conditions, accounting for fluid compressibility. Departing from soil consolidation (Carter and Booker, 1982), Detournay and Cheng (1993) provided governing equations and analytical solutions for different geotechnical problems in deep formations. Their work has been used to benchmark the developments and applications of geomechanical tools in the field of carbon storage (Goerke et al., 2011; Benisch et al., 2013; Jha and Juanes, 2014; Lu and Wheeler, 2020; Camargo et al., 2022; Kachuma et al., 2023), hydrocarbon production (Yin et al., 2007; Roshan and Fahd, 2012; Alpak, 2015; Huang and Ghassemi, 2015; Huang and Ghassemi, 2017) and geothermal exploitation (Zhou and Ghassemi, 2009; Siddiqui and Roshan, 2022; Mutlu et al., 2023).

The governing equations of linear poroelasticity have since been extended to couplings with nonlinear fluid rheology and mechanical behaviors. Within the framework of non-equilibrium thermodynamics, Heidug and Wong (1996) derived a fully coupled chemo-poroelastic model to capture hydration swelling of saturated rocks. Using mixture theory, they established a way to quantify the chemical fluid–solid interactions. In the extension of this chemo-poroelastic theory, thermal effects were incorporated into constitutive equations to estimate the coupled chemo-poro-thermoelastic effects on the perturbations of pore pressure and in-situ stresses in the near wellbore region (Ghassemi et al., 2009; Zhou and Ghassemi, 2009; Liu et al., 2022). To account for the effects of adsorbed gas on matrix deformations, nonlinear constitutive models were constructed to simulate gas transportation in hydrocarbon-bearing formations (Zhao et al., 2004; Zhang et al., 2008; Huang and Ghassemi, 2015). To assess the stability of inclined wellbores, transverse isotropic poroelastic solutions were proposed by Abousleiman and Cui (1998). These studies paved the way to a theoretical framework for simulating single-phase flow in deformable porous media. However, they deal with linear elasticity only, an easy form to implement for underground deformations. Linear elasticity models are not accurate enough for predicting mechanical deformations and rock strength changes around injection and legacy wells during long operations (Zhou and Ghassemi, 2009; Alpak, 2015; Mutlu et al., 2023).

Deep geological formations can exhibit inelastic behaviors (plastic, viscoelastic, or viscoplastic) depending on local properties and loading conditions (Jaeger and Cook, 1979; Colmenares and Zoback, 2002; Bui et al., 2014; Chen and Abousleiman, 2017; Huang and Ghassemi, 2017; Xie et al., 2019). In the near-well regions of both injection and abandoned wells, stress concentrations and induced damages challenge well integrity and operation strategies (Liu et al., 2021; Joulin et al., 2022; Mutlu et al., 2023). To mitigate operational issues, various elasto-plastic models were proposed to assess wellbore stability and casing deformations during injections or depletions (Wang and Samuel, 2016; Xie et al., 2019; Joulin et al., 2022; Sun et al., 2022). Compared to linear elastic models, elasto-plastic models provide a more accurate description of the mechanical behaviors of underground formations. If the stress levels are lower than the yield strength, elastic deformations suffice to predict changes in rock size and shape. However, beyond the yield strength, irreversible and time-dependent changes to microstructures call for plastic or viscoplastic deformation models (Bui et al., 2014; Xie et al., 2019). Elasto-plastic models are therefore necessary to predict the temporal and spatial mechanical responses in the near-wellbore regions and across storage sites (Alpak, 2015; Chen and Abousleiman, 2017; Huang and Ghassemi, 2017; Liu et al., 2021; Mutlu et al., 2023).

Several elasto-plastic models have been developed for specific lithologies or loading conditions (Maiolino and Luong, 2009; Colmenares and Zoback, 2002; Aublivé-Conil et al., 2020). Most models derive from the generalized theory of Mohr-Coulomb (Mohr, 1900). A linear form of the Mohr–Coulomb failure criterion has, for instance, been developed and applied for modelling deformations of various soils and rocks (Jaeger and Cook, 1979; Mogi, 2007). In this model, the yield strength was defined as a function of a cohesion criterion and a friction angle. These two properties are measured from triaxial tests (Colmenares and Zoback, 2002; Mogi, 2007). However, the yield function was assumed independent of the mean stress, ignoring the impact of the intermediate principal stress on the yield strength (Labuz and Zang, 2012; Pan et al., 2016; Liu et al., 2021). Consequently, the deviatoric shape of the Mohr-Coulomb yield surface (the boundary between plastic and elastic regions) is an irregular hexagon (Colmenares and Zoback, 2002;

Conil et al., 2004; Maiolino and Luong, 2009). Working on a yield surface with sharp corners degrades the convergence of numerical models of Mohr-Coulomb (Conil et al., 2004; Labuz and Zang, 2012).

To overcome this numerical obstacle, a dependence of the yield strength on hydrostatic stress levels was introduced in the Drucker-Prager model (Drucker and Prager, 1952; Armero, 1999; Alejano and Bobet, 2012; Vilarrasa, 2014; Singh et al., 2019; Liu et al., 2020). In this model, the yield strength is governed by the deviatoric and hydrostatic stress (the first two stress invariants). In the stress space, the yield surface forms a cone whose deviatoric shape is a circle (Maiolino and Luong, 2009; Alejano and Bobet, 2012). Originally, the Drucker-Prager model was expressed in a linear form. It was then extended into exponential and hyperbolic forms (Alejano and Bobet, 2012). Then, to account for pore collapse under volumetric compression, different cap models were added to the Drucker-Prager yield surface (Lubarda et al. 1996; Choo and Sun, 2018; Liu et al., 2021). Finally, the compressive failure and pressure dependence of elastic properties were captured in the Modified Cam-Clay model, originally developed for saturated soils (Borja et al., 1997; Charlez, 1997). In all these enrichments, Drucker-Prager models have smooth yield surfaces and good numerical behaviors. They are thus common in reservoir simulations (Armero, 1999; Conil et al., 2004; Alpak, 2015).

Drucker–Prager model and its extensions have been applied to geomechanical problems for a variety of materials, including both soil and rocks (Colmenares and Zoback, 2002). Several subsurface energy production and underground storage problems have been handled with this elastoplastic constitutive model, including reservoir compaction, wellbore stability, fracture propagation, fault stability and caprock integrity. Armero (1999) proposed a formulation and finite element implementation of coupled poroplasticity based on stable staggered schemes. An associated Drucker-Prager model was chosen to mimic soil consolidation and compression tests. Based on triaxial compression tests and non-associated Drucker-Prager criterion, Conil et al. (2004) developed an anisotropic poroplastic damage model to simulate material degradations of claystone considering the influence of anisotropic microcracks on the poromechanical coupling. Vilarrasa (2014) evaluated caprock integrity during CO_2 injection by adopting the Drucker-Prager failure criterion at different stress regimes. He concluded that the fluid pressure evolution and its impact on caprock stability varies significantly if injecting through horizontal or vertical wells. Chen and Abousleiman (2017) analytically solved the tunnel excavation and related wellbore stability problems with both friction hardening and hardening-softening Drucker-Prager models. The same wellbore problem was numerically handled by Liu and Chen (2017), who employed a Drucker-Prager model with a return mapping scheme. White et al. (2018) developed a compositional reservoir simulator coupled with a hardening Drucker-Prager model for predicting wellbore failure and modeling field scale CO_2 storage. Choo and Sun (2018) coupled a phase field approach with a Drucker–Prager model to capture the mechanical transition between brittle failure and ductile flow for geomaterials subject to loading and reservoir conditions typically encountered in subsurface energy production and CO_2 sequestration. To allow yield under hydrostatic stress, a compression cap model was incorporated into the original Drucker-Prager model. Similarly, Liu et al. (2021) combined a Drucker–Prager model with a cap plasticity model to explore the mechanical stability of production wells drilled in shallow sediments, which were characterized as weakly consolidated or even unconsolidated formation. Sun et al. (2024) developed an analytical wellbore stability model to investigate casing-reservoir interaction during hydrate depressurization production. In their work, a modified Drucker-Prager model with cohesion weakening caused by hydrate decomposition was considered.

When loading rock samples beyond the yield strength, stress-strain curves move either up or down, indicating irreversible changes in rock strength. Multiple hardening laws (Charlez, 1997; Armero, 1999; Liu and Chen, 2017; Choo and Sun, 2018), or softening laws (Roshan and Fahad, 2012; Lv et al., 2019; Guan et al., 2022) enrich elasto-plastic models to represent this strain strengthening or weakening behavior. These laws correlate changes in shape and position of yield surfaces to the plastic strain and to several other variables such as the cohesion, friction angle or dilatancy coefficient (Armero, 1999; Conil et al., 2004; Choo and Sun, 2018; Liu et al., 2021; Lu et al., 2022). The Drucker-Prager model with friction hardening was used to analytically solve the tunnel excavation problem (Chen and Abousleiman, 2017). In their model, the initial position of the failure envelope is determined by the initial cohesion and friction angle, and its slope depends on the internal friction angle, a quantity linearly related to the accumulated plastic strain and capped by the residual value. Their analytical solution has then been verified by solving the same problem using a finite element model (Liu and Chen, 2017). In our work, we have implemented this elastoplastic model with strain hardening to simulate the inelastic response of underground formations when injecting CO_2. We verify our numerical results with the analytical solution of Chen and Abousleiman (2017).

To have a better understanding of the coupling effects between rock deformations and pore fluid diffusion, the elastoplastic nonlinear mechanical behaviors are added into Biot's theory (Abousleiman et al., 1993; Yale, 2002; Roshan and Fahad 2012; Huang and Ghassemi, 2017; White et al., 2017; Tsopela et al., 2022). These coupled poromechanical models were developed for porous media saturated with a single-phase fluid (Yin et al., 2007; Bui et

al., 2014; Jha and Juanes, 2014). Considering the existence of multiphase mixtures (gas/oil/water) in underground geological formations, a more general theory is required for modeling geological carbon storage (Goerke et al., 2011; Jha and Juanes, 2014; Pan et al., 2016; Shi and Durucan, 2019; Bui et al., 2020; Camargo et al., 2022; Tsopela et al., 2022). Poromechanical coupling with multiple phases create stronger nonlinearity effects (Shi and Durucan, 2019). Multiphase flow, fluid saturation, phase compressibility, capillary effect, gas adsorption and desorption, pore size, pore connection, and compaction have a cumulative impact on pore fluid movements in the pore space and into faults and fractures (Jha and Juanes, 2014; Onishi et al., 2019). These displacements of reservoir fluids and their compression (or expansion) cause stress changes and induce mechanical deformations (Pan et al., 2016). Consequently, inelastic deformations and fault reactivations can occur (Cappa and Rutqvist, 2011; Jha and Juanes, 2014; Liu et al., 2021; Tsopela et al., 2022). Multiphase geomechanical models were used to select monitoring techniques to assess formation uplift and caprock integrity (Camargo et al., 2022). Gas desorption, thermal and chemical interactions can further strengthen coupling effects between fluid flow and rock deformations (Huang and Ghassemi, 2010; Alpak, 2015; Torsæter et al., 2017; Khan et al., 2018; Siddiqui and Roshan, 2022) and affect CO_2 trapping mechanisms (Goerke et al., 2011).

Mechanical deformations of porous media are tightly coupled with fluid flow and transport. To solve poromechanical problems numerically, several coupling schemes have been proposed such as implicit, iterative, explicit, and pseudo (Benisch et al., 2013; Alpak, 2015; Lu and Wheeler, 2020). Among them, fully implicit couplings are used most frequently, with fluid flow and rock deformation equations solved simultaneously (Huang and Ghassemi, 2015; Kachuma et al., 2023). This method requires preconditioners to solve the large ill-conditioned linear systems resulting from the discretization of tightly coupled equations (Lu and Wheeler, 2020). Bui et al. (2020) proposed a scalable physics-based block-triangular preconditioning framework based on Multi-Grid Reduction (MGR) capable of solving basin-scale poromechanical problems. In this work, we use a fully implicit coupling strategy.

To detect operational risks in carbon storage sites, we need a tool that simulates poromechanical deformations of geological formations coupled to the transport of multiphase fluids in the pore space due to CO_2 injection and migration. This is one of the objectives of GEOS, an open source multiphysics numerical simulator (Settgast et al., 2022). In this paper, we benchmark the modeling capabilities, potential applications, and improvements of GEOS in carbon sequestration design and near-wellbore risk analysis. We use the Drucker-Prager model with friction hardening to simulate elastoplastic deformations and a multiphase fluid model with power-law relative permeability to model the migration of a CO_2 plume. Mechanical deformations and fluid flow are coupled in a fully implicit way and solved with MGR preconditioning techniques.

To capture inelastic rock deformation reported in carbon sequestration operations, plastic models have been added to GEOS and coupled with multiphase flow solvers. In the current version of GEOS, we have four elasto-plastic constitutive models: Drucker-Prager with cohesion hardening, extended Drucker-Prager with friction hardening, Modified Cam-Clay, and Delft Egg. The Drucker–Prager model and its extended formulations have been used extensively to solve geomechanical problems including CO2 storage. Therefore, we chose this model for the near-wellbore risk analysis in this study. First, we review the theoretical foundations required to address the geomechanical problems. Then, we show GEOS results for five examples of multiphase flow and wellbore problems with known analytical solutions. This demonstrates the accuracy of the extended Drucker-Prager model and the poromechanical framework. Finally, we present two engineering problems focused on the coupling between mechanical deformation (elastic or plastic) and multiphase fluid flow near CO2 injection wells. From these results, we discuss the advantages and limitations of the extended Drucker-Prager model coupled with multiphase flow. We point out that the poroelastic model with single-phase flow is not capable of predicting the formation of a CO2 plume and of a plastic zone in the vicinity of the injection wells. This highlights the importance of elastoplastic deformations and multiphase flow for modeling CO2 injection and migration in underground formations and demonstrates the applicability of the Drucker-Prager poroplastic model for designing carbon sequestration operations. Our goal for implementing these poroplastic models into GEOS is to run large-scale poromechanical simulations for CO2 storage on distributed, high-performance computing platforms (Camargo et al., 2022; Kachuma et al., 2023). We also offer insights on the impact of plasticity-induced permeability changes and saturation-dependent rock properties, but will address these questions in subsequent works.

2. THEORY

When multiphase fluids flow through a porous medium, spatiotemporal evolutions of rock deformations governed by fluid-fluid and fluid-rock interactions occur. These evolutions have been investigated and simulated at different scales.

The difficulty of modeling multiphase flow in porous medium originates primarily from non-linear couplings between four processes: (i) mechanical deformations of the medium and associated porosity and permeability changes; (ii) fluid flow and induced pore pressure variations; (iii) complex rheology of compositional fluids; (iv) relative permeability of each phase and capillary effects. These non-linear equation systems are closed with conservation laws on mass, force, and energy. The equations governing nonlinear multiphase poromechanics consists of a momentum balance equation and a set of mass balance equations. In this formulation, compressible immiscible two-phase flow and quasi-static small-strain deformation are considered.

For isotropic and isothermal reservoirs without chemical influences, the balance of linear momentum can be written as (Coussy 2004; Bui et al., 2020; Camargo et al., 2022):

$$\nabla \cdot \boldsymbol{\sigma} + \rho_b \boldsymbol{g} = 0 \tag{1}$$

where $\boldsymbol{\sigma}$ represents the Cauchy total stress tensor, $\boldsymbol{g}$ denotes the gravity vector, and the bulk density ρ_b of a porous medium is given as:

$$\rho_b = (1 - \emptyset)\rho_s + \emptyset \sum_\ell \rho_\ell S_\ell \tag{2}$$

where $\emptyset$ is the porosity, ρ_s is the rock density, ρ_ℓ and S_ℓ denote the fluid density and saturation of phase ℓ.

The mass conservation equation for each fluid phase ℓ is expressed as:

$$\frac{dm_\ell}{dt} + \nabla \cdot \boldsymbol{w}_\ell - q_\ell = 0 \tag{3}$$

where m_ℓ represents the mass content of phase ℓ (mass per unit volume of porous medium), $\boldsymbol{w}_\ell$ and q_ℓ denote the mass flux (mass flow rate per unit area) and source term (mass content rate per unit volume) of phase ℓ, which are defined as:

$$m_\ell = \emptyset \sum_\ell \rho_\ell S_\ell \tag{4}$$

$$\boldsymbol{w}_\ell = \sum_\ell \rho_\ell \boldsymbol{v}_\ell \tag{5}$$

where $\boldsymbol{v}_\ell$ is the fluid velocity of phase ℓ. Neglecting capillary pressure, the phase velocity is computed through Darcy's law:

$$\boldsymbol{v}_\ell = -\frac{\boldsymbol{k}k_{r\ell}}{\mu_\ell} \cdot \nabla\left(p_p + \rho_\ell \boldsymbol{g}\right) \tag{6}$$

where p_p is the pore fluid pressure, μ_ℓ is the viscosity of the fluid phase ℓ, $k_{r\ell}$ is the relative permeability of phase ℓ, $\boldsymbol{k}$ is the absolute permeability of the formation. Non-Darcy flow is not considered in this work.

The Brooks-Corey relationship is employed to compute the relative permeabilities of the CO_2-rich phase (k_{rg}) and the aqueous phase (k_{rw}) as a function of the phase saturations (S_g) and (S_w):

$$k_{r\ell} = k^0_{r\ell}(S^*_\ell)^{n_\ell} \tag{7}$$

where $k^0_{r\ell}$ denotes the maximum relative permeability of phase ℓ; n_ℓ is the Corey exponent; the scaled volume fraction (saturation) of phase ℓ is given as:

$$S^*_\ell = \frac{S_\ell - S_{\ell r}}{1 - S_{gr} - S_{wr}} \tag{8}$$

where S_{gr} and S_{wr} are the residual saturations of the CO_2-rich and aqueous phases.

Based on Biot's theory, the constitutive equation is proposed to link the changes in total stress with changes in strain (Detournay and Cheng, 1993; Jha and Juanes, 2014; Huang and Ghassemi, 2015; Cheng, 2016). In incremental form, the effective stress ($\boldsymbol{\sigma}'$) is defined as a function of the total stress ($\boldsymbol{\sigma}$), pore fluid pressure p_p and Biot coefficient (b) (tension is considered positive):

$$\delta\boldsymbol{\sigma} = \delta\boldsymbol{\sigma}' - b\delta p_p \mathbf{1} \tag{9}$$

$$\delta\boldsymbol{\sigma}' = \boldsymbol{C}_{dr} : \boldsymbol{\varepsilon} \tag{10}$$

where $\boldsymbol{C}_{dr}$ denotes drained elasticity tensor; $\mathbf{1}$ represents the identity tensor; $\boldsymbol{\varepsilon}$ is the strain tensor, which can be linked to the displacement vector $\boldsymbol{u}$:

$$\boldsymbol{\varepsilon} = \frac{1}{2}(\nabla \boldsymbol{u} + \nabla^T \boldsymbol{u}) \tag{11}$$

Fluid flow is coupled with mechanics though the change in porosity computed as:

$$\emptyset - \emptyset_0 = b(\varepsilon_v - \varepsilon_{v0}) + \left(\frac{b-\emptyset_0}{K_s}\right)(p_p - p_{p0}) \tag{12}$$

where $\emptyset_0$, ε_{v0}, p_{p0} represent the porosity, volumetric strain, and pore fluid pressure at the reference state respectively; $b = 1 - \frac{K_{dr}}{K_s}$ denotes the Biot coefficient with K_{dr} and K_s representing the drained bulk modulus of the porous medium and the bulk modulus of the solid constituent.

Extending into the plasticity regime with small strain assumption, the total strain $\boldsymbol{\varepsilon}$ is expressed as the sum of elastic ($\boldsymbol{\varepsilon^e}$) and plastic ($\boldsymbol{\varepsilon^p}$) strains:

$$\boldsymbol{\varepsilon} = \boldsymbol{\varepsilon^e} + \boldsymbol{\varepsilon^p} \tag{13}$$

The plastic strain tensor is determined from the flow rule:

$$\delta\boldsymbol{\varepsilon^p} = \Lambda \frac{\partial f}{\partial \boldsymbol{\sigma}} \tag{14}$$

Where Λ is the plastic strain rate and f denotes the plastic potential. Then, the stress-strain relationship is given as:

$$\delta\boldsymbol{\sigma}' = \boldsymbol{C}_{ep} : \delta\boldsymbol{\varepsilon} \tag{15}$$

Where $\boldsymbol{C}_{ep}$ is the stiffness tensor for elasto-plastic materials.

An extended Drucker-Prager model (Chen and Abousleiman, 2017) is implemented into the geomechanical model, whose yield surface is defined as:

$$f(p,q) = q + \beta\left(p - \frac{c_i}{\beta_i}\right) = 0 \tag{16}$$

where p and q represent the mean and deviatoric stress respectively; c_i is the initial cohesion intercept; β and β_i denote the slope of current and initial yield surface in the p – q space, which can be related:

$$\beta = \beta_i + \frac{\lambda}{\varphi+\lambda}(\beta_r - \beta_i) \tag{17}$$

where λ is the accumulated deviatoric plastic strain; φ is a controlling parameter of the hardening rate.

In this plasticity model, the initial position of the yield surface is determined by the initial friction angle and cohesion. With plastic deformations, the friction angle changes (hardens or softens) and asymptotically approaches a residual angle. However, the vertex of the Drucker-Prager cone remains fixed at $p = \frac{c_i}{\beta_i}$ in the p - q space. This way, the cohesion intercept evolves with the friction angle.

In this formulation, changes in the fluid pressure cause an effective stress perturbation and the deformation of the porous medium. Simultaneously, fluid mass transport and pressure evolution are influenced by the mechanical deformation of the porous medium. This formulation has been implemented in GEOS, the open-source high-fidelity numerical simulator employed in this study.

To simplify the problem, here, the thermodynamic behavior of the fluid mixture is described with an immiscible compressible two-phase model. The simulator uses a fully implicit, fully coupled finite element/finite volume approach to simulate multiphase fluid flow and the associated porous rock deformation. The momentum and mass conservation equations are solved on a discretized medium to update simultaneously the mechanical and flow primary variables at each time step. A two-point approximation of the flux (TPFA) is used to discretize the mass flux between cells (Kachuma et al., 2023).

3. VERIFICATION

In this section, the accuracy and applicability of GEOS are demonstrated. First, GEOS results are verified against analytical solutions of two classic consolidation problems and a Buckley-Leverett problem, thus testing poroelasticity

and multiphase flow capabilities. Then, two wellbore cases are simulated to verify the implementation of coupled poroelasticity and plasticity models for operational wellbore problems.

3.1. Terzaghi's consolidation problem

In this first example, we simulate a one-dimensional consolidation problem with simple loading conditions. The analytical solutions of this problem are well-known references and can be used to check the accuracy of numerical predictions (Detournay and Cheng,1993; Ferronato et al., 2010; Huang and Ghassemi, 2017).

Fig.1 shows the setup for this problem, consisting of a poroelastic 1x1x10 m porous column under a constant load and drained through the top surface. Rock properties for this example are listed in Table 1, which corresponds to Ruhr sandstone from literature (Detournay and Cheng, 1993; Cheng, 2016). The column is elastic, homogeneous, isotropic, and fully saturated with fluid. GEOS solves an oedometric deformation in the vertical direction with drainage through the top surface. The lateral surfaces and basement are fixed and impermeable.

A uniform compressive traction of 1.0 MPa is applied instantaneously on the top surface at time $t = 0$. Note that throughout this paper, compressive stresses and strains are negative. Due to coupling effect, the induced overpressure and the corresponding settlement gradually propagate across the poroelastic column. Fig.2 provides comparisons between the numerical simulations from GEOS and the analytical solutions (Detournay and Cheng,1993; Ferronato et al., 2010) on pore pressure (Fig.2a) and vertical displacement (Fig.2b). Our numerical results are in good agreement with the analytical results.

Next, we test the same configuration using different boundary conditions. Instead of a compressive traction, the upper surface is loaded with a constant fluid pressure $p = 1.0$ MPa at time $t = 0$. Like before, we assume that the top surface is the only moving boundary. The analytical solution of this problem was derived by Detournay and Cheng (1993). In Fig.3, the pore pressure and vertical displacement along depth are solved by GEOS and compared to the corresponding analytical solutions. In Fig.3a, the pore pressure within the column increases with time until reaching the constant value at the top surface. The increase of pore pressure causes a dilation of the porous column. Numerical results match the analytical solutions and confirm the rebound of the top surface and the increase of pore pressure upon fluid loading.

These two tests show that GEOS matches analytical responses for oedometric deformations and elastic responses of a simple porous media. In the following sections, we test GEOS on more complex geometries, loading conditions, and mechanical behaviors to compare its numerical results against reference solutions.

3.2. Mandel's Problem

After Terzaghi's consolidation problem, we use GEOS to solve Mandel's 2D consolidation problem, a classic poroelasticity benchmark (Mandel, 1953; Jha and Juanes, 2014; Lu and Wheeler, 2020). This example serves to further verify our implementation of coupled poroelasticity.

As shown in Fig.4, we simulate the consolidation of a poroelastic slab between two rigid and impermeable plates subject to a constant normal force. The slab is fully saturated, homogeneous, isotropic, and infinitely long in the y-direction. A uniform compressive load is applied in the vertical direction. This force leads to a change of pore pressure and causes mechanical deformations of the sample that evolve with time due to fluid diffusion and coupling effects. The numerical model represents a plane strain deformation and allows lateral drainage without confinement. Only a quarter of the computational domain in the x-z plane is modeled and the rest follows by symmetry. We assume single-phase flow to reproduce the conditions of the analytical solution.

A 1x1x0.1 m slab is discretized with 20x1x20 hexahedra. Mechanical properties are given in Table 2, which represents the sand sample used by Ferronato et al. (2010). A uniform load $F = 10^4$ N/m is applied on the top surface. The analytical solution (Cheng and Detournay, 1988) is used to verify the accuracy of the simulations on induced pore pressure and the corresponding settlement. The lateral surface is traction-free and allows drainage. The remaining parts of the outer boundaries are subject to roller constraints.

We use fully coupled simulations to obtain the temporal and spatial solutions for pore pressure and displacements. On Fig.5, we compare results from GEOS (marks) to the corresponding analytical solution (lines) for pore pressure along the x-direction (Fig.5a) and vertical displacements along the z-direction (Fig.5b). GEOS reliably captures the short-term Mandel-Cryer effect and always shows excellent agreement with the analytical solution.

3.3. Buckley-Leverett Problem

We simulate a core flood experiment representing the immiscible transport of a two-phase flow through a porous medium (Buckley and Leverett, 1942). This benchmark is used to validate numerical tools simulating multiphase flow.

As shown in Fig.6, we model the immiscible displacement of a wetting phase by a non-wetting-phase in a porous core. The domain is horizontal, homogeneous, isotropic, and isothermal. Before injection, the core is saturated with the wetting phase. To match the analytical example configuration, the non-wetting phase is injected from the inlet at a constant flow rate. We assume linear and horizontal flow, incompressible and immiscible phases, negligible capillary pressure and gravitational forces, and no poromechanical effects. Upon injection, the fluid front forms the classical Buckley-Leverett solution, with a traveling shock and a rarefaction wave.

The model dimensions are 0.1x0.1x0.002 m, discretized with 1000x1x1 hexahedra. The domain is initially saturated with brine in a uniform pressure field. A constant injection rate of the non-wetting-phase is applied at the fluid inlet. All input parameters are given in Table 3 and extracted from Ekechukwu et al. (2022). The relative permeabilities for both phases (a CO_2-rich phase and an aqueous phase) are modeled with the power-law Brooks-Corey relation shown in Fig. 7. We use the multiphase flow solver in GEOS to obtain the temporal evolution of saturations along the flow direction and verify the solution against Buckley-Leverett analytical solutions (Buckley and Leverett, 1942; Arabzai and Honma, 2013).

Fig.8 compares the results from GEOS (dashed curves) to the corresponding analytical solution (solid curves) for the change of phase saturation for the non-wetting phase (S_g) along the flow direction. The simulation results match the analytical solution in the formation and the progress of a sharp front in the saturation profiles. We conclude that GEOS reliably captures the immiscible transport of two-phase flow.

3.4. Wellbore Problem with Single Phase Flow

In this example, we compute the deformation of rocks near a vertical well using a fully coupled flow and geomechanical model implemented in GEOS. We assume single-phase flow and elastic deformations to match the specifications of the reference analytical solution (Carter and Booker, 1982; Detournay and Cheng, 1993; Cheng, 2016).

The well is vertical, drilled in a porous material, and subject to a non-hydrostatic horizontal stress (σ_h and σ_H) and vertical stress (σ_v), as shown in Fig.9. By changing the traction and pore pressure on the wellbore wall at $t = 0^+$, a mechanical deformation of the reservoir rock is induced under plane strain condition. This deformation evolves with time, due to the coupling with fluid diffusion. Simulations with GEOS are obtained with the parameters in Table 4. The sandstone in the consolidation example is also used for this analysis, and its mechanical properties are provided in Table 1. We compare numerical simulation results to analytical solutions (Carter and Booker, 1982; Detournay and Cheng, 1993).

As shown in Fig.10, the model dimensions are 10x5x2 m with a vertical wellbore of 0.1 m initial radius. We simulate only half of the rock domain and assume symmetry. All the numerical elements are hexahedra, and a refinement is performed to conform to the wellbore geometry. The model is initialized with anisotropic in-situ stresses and zero initial pore pressure. A compressive traction and fluid loading (10 MPa) are applied at the wellbore wall. Three different loading modes are simulated with analytical solutions (Carter and Booker, 1982; Detournay and Cheng, 1993; Cheng, 2016). The outer boundaries are subject to roller and no-flow conditions.

Figs. 11 and 12 show comparisons between GEOS results (marks) and analytical solutions (solid curves) for pore pressure, radial displacement, and effective radial and tangential stresses along the minimum and maximum horizontal stress directions. The dimensionless time is defined as $t^* = ct/a^2$ with $c = 5.2 \times 10^{-3}$ m^2/s.

All the results confirm that the poroelastic coupling effects are accurately captured by GEOS. Wellbore problems with various boundary conditions are also correctly simulated. GEOS can thus be trusted to assess stress states and help design wells and fluid injection schemes for optimal stability.

3.5. Wellbore Contraction Problem with Plasticity

This example illustrates the use of the extended Drucker-Prager elastoplastic model to simulate irreversible deformations near a vertical well. We compare GEOS numerical results against a reference analytical solution (Chen and Abousleiman, 2017).

We use a drained wellbore subject to isotropic horizontal stress (σ_h) and vertical stress (σ_v). By lowering the wellbore supporting pressure (p_p), the wellbore contracts, and the reservoir rock undergoes elastoplastic deformation. A plastic zone develops in the near-wellbore region. To simulate this phenomenon, the strain hardening extended Drucker-Prager model with an associated plastic flow rule is used in GEOS. To mimic the conditions of the analytical solution, only mechanical deformations are considered, and fluid flow is excluded.

The mesh shown in Fig.8 is used. Table 5 summarizes the mechanical properties and loading conditions, which are adopted from Chen and Abousleiman (2017). The model is initialized with an isotropic horizontal stress (11.25 MPa) and vertical stress (15.0 MPa). To reach equilibrium, a compressive traction (11.25 MPa) is instantaneously applied at the wellbore wall at time $t = 0$ s and is gradually reduced to a lower value of 2.0 MPa to let the wellbore contract. The outer boundaries are subject to roller constraints.

Displacement and stress fields around the wellbore are simulated and compared with the analytical solutions. When reducing the wellbore pressure to 2 MPa, Fig.13 shows the modeling predictions for the distributions of normal stress components (radial, tangential, and vertical stresses) along the radial distance normalized to the wellbore radius. Substantial relaxations of these stress components (reduction in their magnitudes) are observed near the wellbore, indicating the development of a plastic zone. The boundary between the elastic and plastic regions are marked by the red dashed line in Fig.13.

Fig.14 shows the numerical results for the stress path in the p - q space for a point on the wellbore wall. During drilling, the reservoir rock initially experiences elastic deformations. The stress path moves vertically until hitting the initial yield surface (blue dashed line). Following that, plastic hardening occurs, and the yield surface expands to accommodate stress changes. Finally, the stress path approaches the residual yield surface (yellow dashed line) and heads toward the vertex of the Drucker-Prager cone.

Variations in the wellbore radius with changes of pressures are plotted in Fig.15. Initially, a linear reduction of the wellbore radius is observed when decreasing wellbore support pressure. After reaching the yield point (red point in Fig. 15), plastic deformations cause a rapid exponential decay of the wellbore radius, matching the analytical solution.

The comparisons between numerical results and analytical solutions in Fig.13, 14, and 15 confirm that the predictions obtained using GEOS match the analytical results. The numerical model can be used as a base for more complex analysis, such as wellbore drilling, fluid injection and storage scenarios.

4. APPLICATION

In fully coupled geomechanics and flow problems, analytical solutions for stress states and reservoir responses can be derived for simplistic scenarios. They do not extrapolate to cases of practical complexity, such as modeling a CO_2 plume migration with mechanical deformations of the reservoir and its surroundings in a realistic geological setting. Moreover, these analytical solutions are only applicable for the scenarios in which some of the coupling between the underlying physics (fluid flow, matrix deformation and rock failure) are simplified, or ignored. Closed-form analytical solutions accounting for all aforementioned coupling processes are not available – numerical methods must be used to solve them. In this section, a multiphase wellbore problem with poroplasticity and a reservoir scale simulation with an egg-shaped aquifer are shown to demonstrate such complex coupling capabilities in GEOS and quantify the impact of elastoplastic deformation and coupling effect in the vicinity of CO_2 injectors.

4.1. Wellbore Scale Problem

Instead of limiting the simulation to single-phase flow, the wellbore problem in Section 3.4 is extended to a poroelastic case with multiphase flow, representing CO_2 injection and immiscible transport of two-phase flow near the injector.

First, we compare the poroelastic models using multiphase flow and single-phase flow to demonstrate the impacts of multiphase flow in reservoir responses during CO_2 injection. We use the mesh shown in Fig.10 and assume isothermal conditions and immiscible two-phase flow for the case with multiphase flow. Modelling parameters are given in Table 4 and mechanical properties of the reservoir rock are provided in Table 1, representing Ruhr sandstone (Detournay and Cheng, 1993; Cheng, 2016). In the case with multiphase flow, the relative permeabilities for both phases (CO_2-rich phase and an aqueous phase) are described with the power-law Brooks-Corey correlation ($n_g = n_w = 2.0$, $S_{gr} = 0.05$, $S_{wr} = 0.3$). Capillary effects are not considered. Constant and identical reservoir permeability and rock properties are assumed for both cases. The domain is initially saturated with brine in a uniform pressure field (1 MPa), and pure CO_2 is injected at the wellbore wall at a constant pressure (10 MPa). We use both the single-phase flow and multiphase flow model to estimate the pore pressure, displacements, and stress fields around the injection well.

Fig.16 shows the evolutions of the pore pressure (p_p) along the radial distance, plotted for multiple values of the dimensionless time $t^* = ct/a^2$ and the dimensionless coordinate $r_d = r/a_0$. As indicated in Fig.16, the pore pressure front radiates away from the injector and the pore pressure near the injector increases with time for both cases. The

corresponding results for the distribution of the radial displacements (Fig.17), radial (Fig.18) and tangential (Fig.19) effective stresses are also plotted and compared between the poroelastic cases with multiphase flow and single-phase flow. These comparisons include the mechanical deformations along both the minimum and maximum horizontal stress directions. Initially (at $t^* = 5.0$), nearly identical results for pore pressure and mechanical variables are obtained; however, after that time, differences between the poroelastic models with multiphase flow and single-phase flow increase with time. Similar trends are observed along all directions.

Discrepancies between poroelastic models using multiphase and single-phase flow formulations are highlighted. In the multiphase flow model, each phase has its own properties (phase viscosity and permeability) and the relative permeabilities for both phases are not constant. They depend on saturation, and hence also time. In the single-phase model, constant fluid properties are assumed. Therefore, the single-phase flow model is inadequate for solving the mechanical deformation here.

Next, we test the linear poroelastic model and a full non-linear poroplastic model with multiphase flow. We compare poroelastic and poroplastic deformations and highlight the important effects of plasticity in CO_2 injections. The geometric settings, fluid properties, and loading conditions are kept the same as those of the previous case. Table 6 summarizes the mechanical properties for the poroplastic case, whose elastic parameters correspond to Ruhr sandstone (Detournay and Cheng, 1993; Cheng, 2016) and plastic parameters are extracted from Chen and Abousleiman (2017). In this configuration, the deformation of the rock can be either poroelastic or poroplastic. We use both a linear elastic isotropic model and an extended Drucker-Prager poroplastic model to compute the pore pressure, displacements, and stress fields around the well.

Fig.20 and 21 show the evolutions of the saturation of CO_2-rich phase (S_g) and pore pressure (p_p) along the radial distance. These two fields are plotted for several values of the dimensionless time $t^* = ct/a^2$ and the dimensionless coordinate $r_d = r/a_0$. As expected in this injection problem, both the saturation front of CO_2-rich phase and pore pressure front radiate away from the well. Therefore, both the CO_2 saturation and the pore pressure in the near wellbore region progressively increase with time. The CO_2 saturation front diffuses slower than the pore pressure front, and the area of the CO_2 plume is smaller than the pore pressure perturbation area. This cannot be predicted by a single-phase formulation. Constant and identical rock permeability values are assumed for both poroelastic and poroplastic cases, so the impact of plasticity on fluid diffusion is excluded in this analysis (Roshan and Fahd, 2012; Alpak, 2015).

GEOS simulation results of the mechanical deformations are shown along the direction of both minimum horizontal stress (σ_h) and maximum horizontal stress (σ_H) for detailed comparisons. The radial displacements (Fig.22), radial (Fig.23) and tangential (Fig.24) effective stresses of the poroplastic case are plotted, together with the corresponding poroelastic values. These comparisons are shown for the displacement and stress profiles along both the minimum and maximum horizontal stress directions. Similar variations are shown along different directions, but differences attributed to stress anisotropy are visible. Because of fluid diffusion and coupling effects, the mechanical variables change over time for both cases.

As shown in Fig.24, relaxations of the tangential stress are detected because of the plastic response of the reservoir rock. Due to stress concentration and CO_2 injection, the stress state in the vicinity of the injecting well did reach the yield strength and forced the surrounding rock to deform plastically, as explained in section 3.5. The formation of this plastic zone is the most important difference between mechanical responses in the near-wellbore region between the two scenarios. In the far-field region, the poroelastic and poroplastic responses become almost identical, and the rock deformations are governed by poroelasticity laws.

We discuss the advantages and limitations of the extended Drucker-Prager poroplastic model coupled with multiphase flow. First, the comparison between poroelastic models with single-phase or multiphase flow formulations shows that a single-phase formulation cannot represent long-term geomechanical deformations accurately. Multiphase formulations give the shape of the CO2 plume over time. This information is necessary to evaluate how the formation responds to the injection. Then, comparing results for poroelastic and poroplastic multiphase models, we observe that the stress state reaches the yield point, and that the plastic behavior dominates mechanical deformations near the wellbore where stress concentrates. This plastic deformation can jeopardize the integrity of injection wells, and elastic models cannot quantify this risk. However, pore pressures and CO2 saturations are almost identical in the poroelastic and poroplastic cases because our models assume a constant matrix permeability and do not include the impact of plasticity on fluid diffusion. These mechanisms could further differentiate poroplastic and poroelastic models. Research along these directions is underway.

4.2. Reservoir Scale Problem

Lastly, we simulate the migration of CO_2 injected into a large-scale aquifer. Using immiscible isothermal two-phase flow and a full poromechanical coupling, we compare poroelastic and poroplastic models. Although we simulate the entire geological domain, we will focus our attention primarily on the near wellbore region.

A synthetic reservoir derived from the "Egg" model is used here to simulate CO_2 injection at field scale. The original Egg model consisted of one reservoir layer and was designed for fluid-only simulations (Jansen et al., 2014). To set up a fully coupled geomechanics and flow simulation of CO_2 injection, we add an overburden, an underburden, and a sideburden, as shown in Fig. 25. We also include one CO_2 injection well, one aquifer and a surrounding aquitard. Fig. 25(a) and 25(b) illustrate the geometry and position of the injector and the aquifer. The egg-shaped aquifer is at the center of the domain (1,181.8x1,181.8x569.4 m). The top of the domain is located at 200 m below ground level, and the depth of the aquifer ranges from 470.7 m to 498.7 m. The entire box-shaped domain consists of 570,000 hexahedra elements of various sizes. As depicted in Fig. 25(c), small elements (8x8x4 m) are used in the target aquifer, and the element size gradually increases when moving away from the aquifer.

The CO_2 and brine phases are assumed immiscible and mutual solubility is excluded. Fluid properties for each phase (density and viscosity) and rock mechanical properties remain constant during the simulation. In both the poroelastic and poroplastic case, the relative permeabilities for both phases (CO_2-rich phase and an aqueous phase) are described using a power-law Brooks-Corey correlation ($n_g = n_w = 2.0$, $S_{gr} = 0.05$, $S_{wr} = 0.3$). Capillary effects are neglected. The domain is isotropic, with different mechanical properties (bulk and shear moduli) and permeabilities assigned for the aquifer and aquitard. For the poroplastic case, only the aquifer experiences plastic deformations (simulated with the extended Drucker-Prager model), and elastic deformations are enforced in the aquitard. All material parameters are summarized in Table 7, representing a sandstone reservoir in the Gulf-of-Mexico (Camargo et al., 2022).

The initial pore pressure is determined by hydrostatic conditions and initial stresses are due to gravity only. At time $t = 0$ s, the reservoir is in hydrostatic equilibrium with a fluid pressure of 2.0 MPa at 200 m depth. The domain is saturated with brine and a uniform value (1.0) of brine saturation is assigned to all layers. For the mechanical equilibrium, a compressive traction (10.0 MPa) is instantaneously applied at the top of the domain at time $t = 0$ s and stress gradients are determined by specified densities and constitutive relationships. The top surface is free to move, and the remaining boundaries are subject to roller constraints. No drainage is allowed through any outer boundary. Prior to simulating the injection, it is necessary to run a few steps of fully coupled geomechanical simulation to reach the equilibrium state. Fig. 26(a) and 26(c) show the spatial distributions of initial pore pressure and effective vertical stress. Tectonic strain is not considered, so the pressure and stress conditions at lateral boundaries are constant over time. Fig. 26(b) shows that no CO_2 exists within the domain after initialization, as expected. After reaching a mechanical equilibrium, we set all displacements to zero, as shown in Fig. 26(d). These initial distributions of pressure, saturation and stress conditions are then used for modeling the subsequent CO_2 injection.

The injection well is vertical and perforated across the entire aquifer interval (470.7 m to 498.7 m). A constant injection rate of CO_2 of 0.1 kg/s is applied for a 6-month period. The initialized poromechanical model is used to predict the migration of the CO_2 plume and the induced rock deformation. The mechanical response of the aquifer is simulated with either a linear elastic model or a poroplastic extended Drucker-Prager model. Fig. 27 shows a cross-section with the pore pressure and CO_2 saturation for both the poroelastic and poroplastic solutions after 6 months. The distribution patterns of CO_2 and pore pressure perturbations obtained from the poroelastic case are similar to those from the poroplastic case. Upon injection, both the saturation front of CO_2 and pore pressure front move away from the injector. Changes in these flow solutions become more noticeable over time, especially in the near wellbore region. Comparing to the area of induced pore pressure (Fig.27(a) and (b)), the area of the CO_2 plume (Fig.27(c) and (d)) is much smaller, and the CO_2 front propagates slower than the pore pressure perturbation. Due to high permeability contrasts between the aquitard and aquifer, the CO_2 plume is safely contained within the target formation. In this example, we see only small differences between the poroelastic and poroplastic solutions. This observation is in agreement with the reference work (Roshan and Fahd, 2012; Alpak, 2015).

CO_2 injection into the porous aquifer increases the pore pressure near the injector, thus reducing the effective stresses and causing matrix dilation. This deformation propagates away from the injection site. In a stiff rock formation, it generates an uplift of the aquifer top. Similar patterns for the distribution of stresses (Fig.28) and displacements (Fig.29) are observed for both poroplastic and poroelastic solutions. Differences between the poroelastic and poroplastic solutions are visible on the mechanical responses in the near wellbore region. Fig. 28 shows the 3D view of the effective vertical stress after six months for the poroelastic and poroplastic cases. Fig. 28(c) compares

poroplastic and poroelastic solutions for the effective vertical stress along a horizontal line at the aquifer top. Relaxations of the effective vertical stress (reduction in the magnitude) are observed around the injection wellbore, indicating the development of a plastic zone. Fig. 29 shows the vertical displacements for the poroelastic and poroplastic cases. Fig. 29(c) plots the poroplastic and poroelastic solutions of the vertical displacements on top of the aquifer. Due to the reservoir and injection conditions, the stress state close to the injector reaches the yield strength in the poroplastic model and induces a plastic deformation of the surrounding rock. Consequently, in the plastic case, lower vertical displacements on the top of the aquifer are expected.

As a summary, in this example, we have injected CO_2 into a large aquifer initially at mechanical equilibrium, and we have tested how the rock deforms in a poroelastic and a poroplastic scenario. Initially, the differences are visible mostly near the injection site, consistently with the example in section 4.1. We see that in both scenarios, the injection and plume migration create pressure build-ups that trigger mechanical deformations over the entire domain. With time, the plastic zone expands away from the well and the differences between poroelastic and poroplastic models amplify. Ignoring plastic deformations will, therefore, lead to inaccurate predictions of near-wellbore and long-term states, underestimating integrity risks (Liu et al., 2021). The multiphase poromechanics simulation shown here can be extended to various operational scenarios (excavation, depletion, injection, and pressurization), where the coupling between multiphase flow and geomechanical deformations plays a key role.

Table 8 is added to summarize the number of elements, number of time-steps, time increments, computation times and number of CPUs for all examples. Runs were performed on an internal high-performance computing system (HPC). For simple analytical problems (e.g., consolidation and Mandel problem), the cases would run fine on a consumer-grade desktop. However, field scale simulations (e.g., egg model) benefit from the firepower of distributed HPCs. The objective of implementing these poroplastic models into GEOS is to run large scale simulations (several millions of elements) for CO2 storage in parallel on HPCs (Camargo et al., 2022; Kachuma et al., 2023). Due to time and memory constrains, it is impossible to execute these simulations on a single desktop. The cases shown in this study are used to benchmark the accuracy and applications of the poroplastic models. The efficiency of numerical simulations is beyond the scope of this work and shown here for information only.

5. CONCLUSION

We use GEOS, an open-source, high-fidelity numerical simulator, to detect and mitigate operational risks in geological carbon storage. GEOS uses a fully coupled finite element/finite volume approach to simulate multiphase fluid flow and the associated rock deformations. After verifying the results obtained in five examples with analytical reference solutions, we simulate poromechanical deformations in more complex field-scale problems.

Injecting CO_2 alters stress conditions and fluid phase compositions in the near-well and far-field regions, thus changing their transport and mechanical properties. To simulate these phenomena, we use the Drucker-Prager model with friction hardening and a multiphase fluid model with power-law correlations for relative permeability. We show two engineering problems highlighting the differences between poroelastic and poroplastic behaviors. Both cases demonstrate the importance of poroplastic effects for accurate predictions of mechanical deformations and stress perturbations during CO_2 injection in underground formations.

GEOS can simulate short-term processes near the injectors with coupled stress evolutions, rock deformations, and multiphase compositional flow and transport. GEOS can also simulate similar effects in large-scale, long-term CO_2 storage sites and their surrounding formations. Such large-scale and long-term multiphysics simulations help guide operational decisions for CO_2 injection. In particular, these models help to assess containment potential and wellbore stability during and after CO_2 injection.

In this work, we have considered only isothermal conditions and neglected chemical interactions between rocks and fluids. We will include these thermal and chemical effects in future works.

ACKNOWLEDGEMENTS

The authors would like to thank the GEOS development team. Funding was provided by TotalEnergies through the FC-MAELSTROM project. Portions of this work were performed under the auspices of the U.S. Department of Energy by Lawrence Livermore National Laboratory under Contract DE-AC52-07NA27344.

Declarations

Conflict of interest The authors declare that they have no conflict of interests.

References

Abousleiman Y, Cheng A-D, Jiang C, Roegiers J-C (1993) A micromechanically consistent poroviscoelasticity theory for rock mechanics applications. International Journal of Rock Mechanics and Mining Sciences & Geomechanics Abstracts 30:1177–1180. https://doi.org/10.1016/0148-9062(93)90090-Z

Abousleiman Y, Cui L (1998) Poroelastic solutions in transversely isotropic media for wellbore and cylinder. International Journal of Solids and Structures 35:4905–4929. https://doi.org/10.1016/S0020-7683(98)00101-2

Alejano LR, Bobet A (2012) Drucker–Prager Criterion. Rock Mechanics and Rock Engineering 45:995–999. https://doi.org/10.1007/s00603-012-0278-2

Alpak FO (2015) Robust Fully-Implicit Coupled Multiphase-Flow and Geomechanics Simulation. SPE J. 20:1366–1383. https://doi.org/10.2118/172991-PA

Arabzai A, Honma S (2013) Numerical simulation of the Buckley-Leverett problem. Proceedings of School of Engineering of Tokai University 38:9–14

Armero F (1999) Formulation and finite element implementation of a multiplicative model of coupled poro-plasticity at finite strains under fully saturated conditions. Computer Methods in Applied Mechanics and Engineering 171:205–241. https://doi.org/10.1016/S0045-7825(98)00211-4

Aublivé-Conil N, Djeran-Maigre I, Cabrillac R, Su K (2020) Poroplastic modelling including damage for deep argillaceous rocks. In: Poromechanics II. CRC Press, pp 873–878

Bachu S, Bennion DB (2009) Experimental assessment of brine and/or CO2 leakage through well cements at reservoir conditions. International Journal of Greenhouse Gas Control 3:494–501. https://doi.org/10.1016/j.ijggc.2008.11.002

Benisch K, Graupner B, Bauer S (2013) The Coupled OpenGeoSys-eclipse Simulator for Simulation of CO2 Storage – code Comparison for Fluid Flow and Geomechanical Processes. Energy Procedia 37:3663–3671. https://doi.org/10.1016/j.egypro.2013.06.260

Biot MA (1935) A general property of two-dimensional thermal stress distribution. The London, Edinburgh, and Dublin Philosophical Magazine and Journal of Science 19:540–549. https://doi.org/10.1080/14786443508561399

Biot MA (1941) General Theory of Three-Dimensional Consolidation. Journal of Applied Physics 12:155–164. https://doi.org/10.1063/1.1712886

Borja RI, Tamagnini C, Amorosi A (1997) Coupling Plasticity and Energy-Conserving Elasticity Models for Clays. Journal of Geotechnical and Geoenvironmental Engineering 123:948–957. https://doi.org/10.1061/(ASCE)1090-0241(1997)123:10(948)

Buckley SE, Leverett MC (1942) Mechanism of Fluid Displacement in Sands. Trans. 146:107–116. https://doi.org/10.2118/942107-G

Bui QM, Osei-Kuffuor D, Castelletto N, White JA (2020) A Scalable Multigrid Reduction Framework for Multiphase Poromechanics of Heterogeneous Media. SIAM Journal on Scientific Computing 42:B379-B396. https://doi.org/10.1137/19M1256117

Bui TA, Wong H, Deleruyelle F, Dufour N, Leo C, Sun DA (2014) Analytical modeling of a deep tunnel inside a poro-viscoplastic rock mass accounting for different stages of its life cycle. Computers and Geotechnics 58:88–100. https://doi.org/10.1016/j.compgeo.2013.11.004

Camargo J, Hamon F, Mazuyer A, Meckel T, Castelletto N, White J (2022) Deformation Monitoring Feasibility for Offshore Carbon Storage in the Gulf-of-Mexico. SSRN Electronic Journal. https://doi.org/10.2139/ssrn.4296637

Cappa F, Rutqvist J (2011) Modeling of coupled deformation and permeability evolution during fault reactivation induced by deep underground injection of CO2. International Journal of Greenhouse Gas Control 5:336–346. https://doi.org/10.1016/j.ijggc.2010.08.005

Carter J, Booker J (1982) Elastic consolidation around a deep circular tunnel. International Journal of Solids and Structures 18:1059–1074. https://doi.org/10.1016/0020-7683(82)90093-2

Charlez PA (1997) The impact of constitutive laws on wellbore stability: a general review. SPE Drilling & Completion 12:119–127

Chen SL, Abousleiman YN (2017) Wellbore stability analysis using strain hardening and/or softening plasticity models. International Journal of Rock Mechanics and Mining Sciences 93:260–268. https://doi.org/10.1016/j.ijrmms.2017.02.007

Cheng A-D, Detournay E (1988) A direct boundary element method for plane strain poroelasticity. Int. J. Numer. Anal. Meth. Geomech. 12:551–572. https://doi.org/10.1002/nag.1610120508

Cheng AH-D (2016) Poroelasticity, vol 27. Springer

Choo J, Sun W (2018) Coupled phase-field and plasticity modeling of geological materials: From brittle fracture to ductile flow. Computer Methods in Applied Mechanics and Engineering 330:1–32. https://doi.org/10.1016/j.cma.2017.10.009

Colmenares L, Zoback M (2002) A statistical evaluation of intact rock failure criteria constrained by polyaxial test data for five different rocks. International Journal of Rock Mechanics and Mining Sciences 39:695–729. https://doi.org/10.1016/S1365-1609(02)00048-5

Conil N, Djeran-Maigre I, Cabrillac R, Su K (2004) Poroplastic damage model for claystones. Applied Clay Science 26:473–487. https://doi.org/10.1016/j.clay.2003.12.019

Coussy O (2004) Poromechanics. John Wiley & Sons

Detournay E, Cheng AH-D (1993) Fundamentals of poroelasticity. In: Analysis and design methods. Elsevier, pp 113–171

Drucker DC, Prager W (1952) Soil mechanics and plastic analysis or limit design. Quarterly of Applied Mathematics 10:157–165

Ekechukwu GK, Loubens R de, Araya-Polo M (2022) LSTM-driven Forecast of CO2 Injection in Porous Media. arXiv preprint arXiv:2203.05021

Ferronato M, Castelletto N, Gambolati G (2010) A fully coupled 3-D mixed finite element model of Biot consolidation. Journal of Computational Physics 229:4813–4830. https://doi.org/10.1016/j.jcp.2010.03.018

Gan M, Nguyen MC, Zhang L, Wei N, Li J, Lei H, Wang Y, Li X, Stauffer PH (2021) Impact of reservoir parameters and wellbore permeability uncertainties on CO2 and brine leakage potential at the Shenhua CO2 Storage Site, China. International Journal of Greenhouse Gas Control 111:103443. https://doi.org/10.1016/j.ijggc.2021.103443

Ghassemi A, Tao Q, Diek A (2009) Influence of coupled chemo-poro-thermoelastic processes on pore pressure and stress distributions around a wellbore in swelling shale. Journal of Petroleum Science and Engineering 67:57–64. https://doi.org/10.1016/j.petrol.2009.02.015

Goerke U-J, Park C-H, Wang W, Singh A, Kolditz O (2011) Numerical Simulation of Multiphase Hydromechanical Processes Induced by CO2 Injection into Deep Saline Aquifers. Oil & Gas Science and Technology – Rev. IFP Energies nouvelles 66:105–118. https://doi.org/10.2516/ogst/2010032

Guan K, Zhang Q, Liu H, Zhu W (2022) A New Numerical Procedure for the Excavation Response in Mohr–Coulomb Rock Mass Exhibiting Strain-Softening Behavior. Frontiers in Earth Science 10. https://doi.org/10.3389/feart.2022.872792

Heidug WK, Wong S-W (1996) Hydration swelling of water-absorbing rocks: A constitutive model. Int. J. Numer. Anal. Meth. Geomech. 20:403–430. https://doi.org/10.1002/(SICI)1096-9853(199606)20:6<403:AID-NAG832>3.0.CO;2-7

Huang J, Ghassemi A (2010) A Chemo-poroelastic Solution For Pore Pressure Transmission Test Considering Solute Diffusion. In: ARMA-10-337

Huang J, Ghassemi A (2015) A poroelastic model for evolution of fractured reservoirs during gas production. Journal of Petroleum Science and Engineering 135:626–644. https://doi.org/10.1016/j.petrol.2015.10.007

Huang J, Ghassemi A (2017) Poro-viscoelastic modeling of production from shale gas reservoir: An adaptive dual permeability model. Journal of Petroleum Science and Engineering 158:336–350. https://doi.org/10.1016/j.petrol.2017.08.046

Jaeger JC, Cook N (1979) Fundamentals of Rock Mechanics. Science paperbacks. Springer Netherlands

Jansen JD, Fonseca RM, Kahrobaei S, Siraj MM, van Essen GM, van den Hof PMJ (2014) The egg model – a geological ensemble for reservoir simulation. Geosci. Data J. 1:192–195. https://doi.org/10.1002/gdj3.21

Jha B, Juanes R (2014) Coupled multiphase flow and poromechanics: A computational model of pore pressure effects on fault slip and earthquake triggering. Water Resour. Res. 50:3776–3808. https://doi.org/10.1002/2013WR015175

Joulin C, Lagarde F, Le Goff T-H, Pauget L, Benmesbah MO, Su K, Poyol E (2022) Advanced Well Integrity Experiment and Tools to Repurpose Legacy Wells for CO2 Injection. Available at SSRN 4285287

Kachuma D, Ramsay T, Gross H, Kloucha C, Hamon F, Gacem M, Jellema R, Noushabadi MJ (2023) Assessment of CO2 Storage Capacities and Identification of Operational Risks Using Large Basin-Scale Multi-Physics Simulation. In: D021S069R002

Khan S, Khulief YA, Al-Shuhail AA (2018) The effect of injection well arrangement on CO2 injection into carbonate petroleum reservoir. International Journal of Global Warming 14:462–487. https://doi.org/10.1504/IJGW.2018.091532

Labuz JF, Zang A (2012) Mohr–Coulomb Failure Criterion. Rock Mechanics and Rock Engineering 45:975–979. https://doi.org/10.1007/s00603-012-0281-7

Liu C, Han Y, Phan DT, Abousleiman YN (2022) Stress solutions for short- and long-term wellbore stability analysis. Journal of Natural Gas Science and Engineering 105:104693. https://doi.org/10.1016/j.jngse.2022.104693

Liu K, Chen SL (2017) Finite element implementation of strain-hardening Drucker–Prager plasticity model with application to tunnel excavation. Underground Space 2:168–174. https://doi.org/10.1016/j.undsp.2017.08.003

Liu K, Chen SL, Gu XQ (2020) Analytical and Numerical Analyses of Tunnel Excavation Problem Using an Extended Drucker–Prager Model. Rock Mechanics and Rock Engineering 53:1777–1790. https://doi.org/10.1007/s00603-019-01992-5

Liu W, Lin H, Liu H, Luo C, Wang G, Deng J (2021) Numerical Investigation of Wellbore Stability in Deepwater Shallow Sediments. Geofluids 2021:1–14

Lu D, Su C, Zhou X, Wang G, Du X (2022) A cohesion-friction combined hardening plastic model of concrete with the nonorthogonal flow rule: Theory and numerical implementation. Construction and Building Materials 325:126586. https://doi.org/10.1016/j.conbuildmat.2022.126586

Lu X, Wheeler MF (2020) Three-way coupling of multiphase flow and poromechanics in porous media. Journal of Computational Physics 401:109053. https://doi.org/10.1016/j.jcp.2019.109053

Lubarda VA, Mastilovic S, Knap J (1996) Brittle-Ductile Transition in Porous Rocks by Cap Model. Journal of Engineering Mechanics 122:633–642. https://doi.org/10.1061/(ASCE)0733-9399(1996)122:7(633)

Lv A, Masoumi H, Walsh SDC, Roshan H (2019) Elastic-Softening-Plasticity Around a Borehole: An Analytical and Experimental Study. Rock Mechanics and Rock Engineering 52:1149–1164. https://doi.org/10.1007/s00603-018-1650-7

Maiolino S, Luong P (2009) Measuring discrepancies between Coulomb and other geotechnical criteria: Drucker-Prager and Matsuoka-Nakai

Mandel J (1953) Consolidation Des Sols (Étude Mathématique). Géotechnique 3:287–299. https://doi.org/10.1680/geot.1953.3.7.287

Mogi K (2007) Experimental rock mechanics, vol 3. Taylor & Francis, London

Mohr O (1900) Welche Umstände bedingen die Elastizitätsgrenze und den Bruch eines Materials. Zeitschrift des Vereins Deutscher Ingenieure 46:1572–1577

Mutlu O, Ghassemi A, Boitnott G (2023) Near Wellbore Formation Integrity in Sedimentary Geothermal Storage Systems: Insights from THM Models. In: ARMA-2023-0496

Nogues JP, Nordbotten JM, Celia MA (2011) Detecting leakage of brine or CO2 through abandoned wells in a geological sequestration operation using pressure monitoring wells. Energy Procedia 4:3620–3627. https://doi.org/10.1016/j.egypro.2011.02.292

Onishi T, Nguyen MC, Carey JW, Will B, Zaluski W, Bowen DW, Devault BC, Duguid A, Zhou Q, Fairweather SH, Spangler LH, Stauffer PH (2019) Potential CO2 and brine leakage through wellbore pathways for geologic CO2 sequestration using the National Risk Assessment Partnership tools: Application to the Big Sky Regional Partnership. International Journal of Greenhouse Gas Control 81:44–65. https://doi.org/10.1016/j.ijggc.2018.12.002

Pan P, Wu Z, Feng X, Yan F (2016) Geomechanical modeling of CO2 geological storage: A review. Journal of Rock Mechanics and Geotechnical Engineering 8:936–947. https://doi.org/10.1016/j.jrmge.2016.10.002

Rajapakse R. K. N. D. (1993) Stress Analysis of Borehole in Poroelastic Medium. Journal of Engineering Mechanics 119:1205–1227. https://doi.org/10.1061/(ASCE)0733-9399(1993)119:6(1205)

Rice JR, Cleary MP (1976) Some basic stress diffusion solutions for fluid-saturated elastic porous media with compressible constituents. Rev. Geophys. 14:227–241. https://doi.org/10.1029/RG014i002p00227

Roshan H, Fahad M (2012) Chemo-poroplastic analysis of a borehole drilled in a naturally fractured chemically active formation. International Journal of Rock Mechanics and Mining Sciences 52:82–91. https://doi.org/10.1016/j.ijrmms.2012.03.004

Settgast, R. R., Corbett, B. C., Klevtsov, S., Hamon, F., Sherman, C., Cusini, M., Gazzola, T., Tobin, W., White, J.,Castelletto, N., Borio, A., Franceschini, A., Huang, J., Han, B., Gross, H., Franc, J., Mazuyer, A., Besset, J.,

Citrain,A., Vargas, A., Cremon, M., Hao, Y., Khait, M., Lacoste, X., Semnani, S., Frambati, S., N'diaye, M., Nguyen, S., Morgan, H. M. (2022) GEOSX/GEOSX: v0.2.1-alpha. https://doi.org/10.5281/zenodo.7151032

Shi J-Q, Durucan S (2009) A coupled reservoir-geomechanical simulation study of CO2 storage in a nearly depleted natural gas reservoir. Energy Procedia 1:3039–3046. https://doi.org/10.1016/j.egypro.2009.02.082

Siddiqui MAQ, Roshan H (2022) Thermodynamic Characterization of Chemical Damage in Variably Saturated Water-Active Shales. Rock Mechanics and Rock Engineering 55:5259–5284. https://doi.org/10.1007/s00603-022-02916-6

Singh A, Seshagiri Rao K, Ayothiraman R (2019) A Closed-Form Analytical Solution for Circular Opening in Rocks Using Drucker–Prager Criterion. Indian Geotechnical Journal 49:437–454. https://doi.org/10.1007/s40098-019-00358-6

Sun H, Chang Y, Sun B, Wang K, Chen G, Li H, Dai Y (2024) Stability of the wellbore wall during marine hydrate depressurization production based on a modified Drucker-Prager model. Fuel 362:130624. https://doi.org/10.1016/j.fuel.2023.130624

Sun Z, Cosson C, Plougoulen A, Datye D, Fager A, Crouse B (2022) An Integrated Geology-to-Geomechanics Workflow to Assess Geomechanical Risk of CO2 Geological Storage. In: ARMA-2022-0580

Terzaghi K (1925) Erdbaumechanik auf bodenphysikalischer Grundlage. F. Deuticke

Terzaghi K von (1923) Die Berechnug der Durchlassigkeit des Tones aus dem Verlauf der hydromechanischen Spannungserscheinungen. Sitzungsber. Akad. Wiss.(Wien). Math.-Naturwiss. Kl., Abt. Iia 132:125–138

Torsæter M, Todorovic J, Lavrov A, Gawel K, Lund H, Roy P, Carroll S (2017) Avoiding Damage of CO2 Injection Wells Caused by Temperature Variations. Energy Procedia 114:5275–5286. https://doi.org/10.1016/j.egypro.2017.03.1645

Tsopela A, Bere A, Dutko M, Kato J, Niranjan SC, Jennette BG, Hsu S-Y, Dasari GR (2022) CO2 injection and storage in porous rocks: coupled geomechanical yielding below failure threshold and permeability evolution. Petroleum Geoscience 28:petgeo2020-124. https://doi.org/10.1144/petgeo2020-124

Vilarrasa V (2014) Impact of CO2 injection through horizontal and vertical wells on the caprock mechanical stability. International Journal of Rock Mechanics and Mining Sciences 66:151–159. https://doi.org/10.1016/j.ijrmms.2014.01.001

Wang H, Samuel R (2016) 3D Geomechanical Modeling of Salt-Creep Behavior on Wellbore Casing for Presalt Reservoirs. SPE Drill & Compl 31:261–272. https://doi.org/10.2118/166144-PA

White D, Ganis B, Liu R, Wheeler MF (2017) A Near-Wellbore Study with a Drucker-Prager Plasticity Model Coupled with a Parallel Compositional Reservoir Simulator. In: the SPE Reservoir Simulation Conference held in Montgomery, TX, USA, 20–22 February 2017

White JA, Burnham AK, Camp DW (2017) A Thermoplasticity Model for Oil Shale. Rock Mechanics and Rock Engineering 50:677–688. https://doi.org/10.1007/s00603-016-0947-7

Xie X, Fjær E, Detournay E (2019) Time-dependent closure of a borehole in a viscoplastic rock. Geomechanics for Energy and the Environment 19:100115. https://doi.org/10.1016/j.gete.2019.02.001

Yale DP (2002) Coupled Geomechanics-Fluid Flow Modeling: Effects of Plasticity and Permeability Alteration. In: SPE/ISRM Rock Mechanics Conference, SPE-78202-MS

Yin S, Dusseault MB, Rothenburg L (2007) Coupled multiphase poroelastic analysis of reservoir depletion including surrounding strata. International Journal of Rock Mechanics and Mining Sciences 44:758–766. https://doi.org/10.1016/j.ijrmms.2006.11.005

Zhang H, Liu J, Elsworth D (2008) How sorption-induced matrix deformation affects gas flow in coal seams: A new FE model. International Journal of Rock Mechanics and Mining Sciences 45:1226–1236. https://doi.org/10.1016/j.ijrmms.2007.11.007

Zhao Y, Hu Y, Zhao B, Yang D (2004) Nonlinear Coupled Mathematical Model for Solid Deformation and Gas Seepage in Fractured Media. Transport in Porous Media 55:119–136. https://doi.org/10.1023/B:TIPM.0000010679.50682.69

Zhou X, Ghassemi A (2009) Finite element analysis of coupled chemo-poro-thermo-mechanical effects around a wellbore in swelling shale. International Journal of Rock Mechanics and Mining Sciences 46:769–778. https://doi.org/10.1016/j.ijrmms.2008.11.009

Tables and Figures

Bulk Modulus, K	$1.3\text{x}10^{10}$ Pa
Shear Modulus, G	$1.3\text{x}10^{10}$ Pa
Grain Bulk Modulus, K_s	$3.6\text{x}10^{10}$ Pa
Porosity, $\emptyset$	0.02
Fluid Density, ρ_f	1000 kg/m^3
Fluid Viscosity, μ_f	0.001 Pa·s
Fluid Compressibility, c_f	$3.72\text{x}10^{-10}$ Pa^{-1}
Permeability, k	$2.0\text{x}10^{-16}$ m^2
Column Length, L	10.0 m

Table 1 Input parameters for 1D consolidation problem.

Bulk Modulus, K	$6.67\text{x}10^{7}$ Pa
Shear Modulus, G	$4.0\text{x}10^{7}$ Pa
Grain Bulk Modulus, K_s	$1.0\text{x}10^{27}$ Pa
Force per Unit Length, F	-10^{-4} N/m
Porosity, $\emptyset$	0.375
Fluid Density, ρ_f	1000 kg/m^3
Fluid Viscosity, μ_f	0.001 Pa·s
Fluid Compressibility, c_f	$4.4\text{x}10^{-10}$ Pa^{-1}
Permeability, k	10^{-12} m^2
Slab Length, $2a$	2.0 m
Slab Height, $2b$	2.0 m

Table 2 Input parameters for Mandel's problem.

Max Relative Permeability of Gas, k_{rg}^0	1.0
Max Relative Permeability of Water, k_{rw}^0	1.0
Corey Exponent of Gas, n_g	3.5

Corey Exponent of Water, n_w	3.5
Residual Gas Saturation, S_{gr}	0.0
Residual Water Saturation, S_{wr}	0.0
Porosity, $\emptyset$	0.2
Permeability, k	9.0×10^{-13} m^2
Gas Viscosity, μ_g	2.3×10^{-5} Pa·s
Water Viscosity, μ_w	5.5×10^{-4} Pa·s
Total Flow Rate, Q_T	2.5×10^{-7} m^3/s
Domain Length, D_L	0.1 m
Domain Width, D_W	1.0 m
Domain Thickness, D_T	0.002 m

Table 3 Input parameters for the Buckley-Leverett problem.

Minimum Horizontal Stress, σ_h	9.0×10^6 Pa
Maximum Horizontal Stress, σ_H	1.1×10^7 Pa
Vertical Stress, σ_v	1.2×10^7 Pa
Initial Wellbore Radius, a_0	0.1 m
Traction at Wellbore, τ_w	1.0×10^7 Pa
Fluid Pressure at Wellbore, p_p	1.0×10^7 Pa

Table 4 Input parameters for the single-phase wellbore problem.

Bulk Modulus, K	5.0×10^8 Pa
Shear Modulus, G	3.0×10^8 Pa
Cohesion, C	0.0 Pa

Initial Friction Angle, $\emptyset_i$	15.27 Degree
Residual Friction Angle, $\emptyset_i$	23.05 Degree
Hardening Rate, c_h	0.01
Horizontal Stress, σ_h	1.125×10^7 Pa
Vertical Stress, σ_v	1.5×10^7 Pa
Initial Wellbore Radius, a_0	0.1 m
Fluid Pressure at Wellbore, p_p	2.0×10^6 Pa

Table 5 Input parameters for the wellbore contraction problem with plasticity.

Bulk Modulus, K	1.3×10^{10} Pa
Shear Modulus, G	1.3×10^{10} Pa
Cohesion, C	1.0×10^6 Pa
Initial Friction Angle, $\emptyset_i$	15.0 Degree
Residual Friction Angle, $\emptyset_i$	23.0 Degree
Hardening Rate, c_h	0.01
Reservoir Permeability, k	2.0×10^{-16} m^2
CO_2 Density, ρ_{co2}	848 kg/m^3
Brine Density, ρ_{brine}	1173 kg/m^3
CO_2 Viscosity, μ_{co2}	8.1×10^{-5} Pa·s
Brine Viscosity, μ_{brine}	1.0×10^{-3} Pa·s

Table 6 Input parameters for the poroplastic case.

Bulk Modulus of Aquifer, K	9.4×10^9 Pa
Shear Modulus of Aquifer, G	5.64×10^9 Pa

Cohesion of Aquifer, C	2.0x10^{6} Pa
Initial Friction Angle of Aquifer, $\emptyset_i$	15.0 Degree
Residual Friction Angle of Aquifer, $\emptyset_i$	20.0 Degree
Hardening Rate of Aquifer, c_h	0.01
Porosity of Aquifer, $\emptyset$	0.2
Permeability of Aquifer, k	1.0x10^{-15} m^2
Bulk Modulus of Burdens, K_B	1.15x10^{10} Pa
Shear Modulus of Burdens, G_B	5.31x10^{9} Pa
Porosity of Burdens, $\emptyset_B$	0.05
Permeability of Burdens, k_B	1.0x10^{-18} m^2
Grain Bulk Modulus, K_s	1.0x10^{27} Pa
Rock Density, ρ_r	2700 kg/m^3
CO_2 Density, ρ_{co2}	479 kg/m^3
Brine Density, ρ_{brine}	1045 kg/m^3
CO_2 Viscosity, μ_{co2}	3.95x10^{-5} Pa·s
Brine Viscosity, μ_{brine}	2.535x10^{-4} Pa·s
Injection Rate, q_{inj}	0.1 kg/s

Table 7 Input parameters for the Egg model.

Cases	3.1-traction loading	3.1-fluid loading	3.2	3.3	3.4	3.5	4.1-elastic with single-phase	4.1-elastic with multi-phase	4.1-plastic with multi-phase	4.2-elastic with multi-phase	4.2-plastic with multi-phase
Number of Elements	25	25	400	1,000	16,000	16,000	16,000	16,000	16,000	570,000	570,000
Number of Time Steps	901	901	405	7078	1008	54	101	133	128	36	36
Time Increment (s)	10	10	0.025	0.01	0.00969	0.02	9.69	9.69	9.69	1,000,000	1,000,000
Computational Time (s)	6.9	5.5	97.0	185.0	3378.3	13.3	428.9	366.7	373.2	627.7	556.9
Number of CPUs	1	1	1	1	16	1	16	16	16	128	128

Table 8 Numerical settings and computational time for all presented examples.

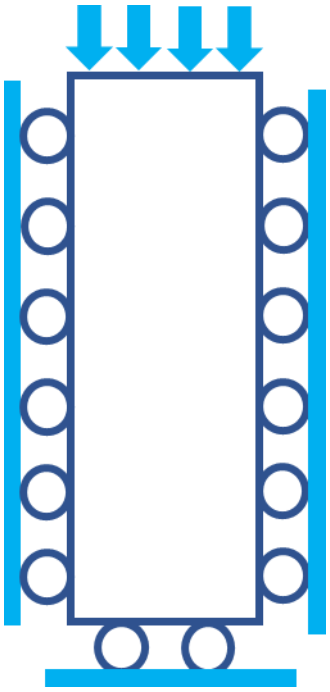

Fig.1 Sketch of the setup for 1D consolidation problem.

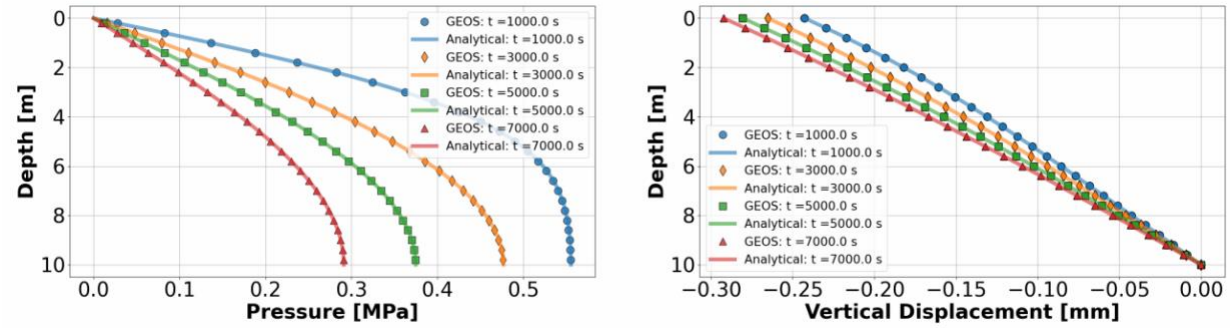

Fig.2 Comparisons between GEOS numerical results (marker) and analytical solutions (lines) for the 1D consolidation problem subject to traction loading: (a) pore pressure; (b) vertical displacement.

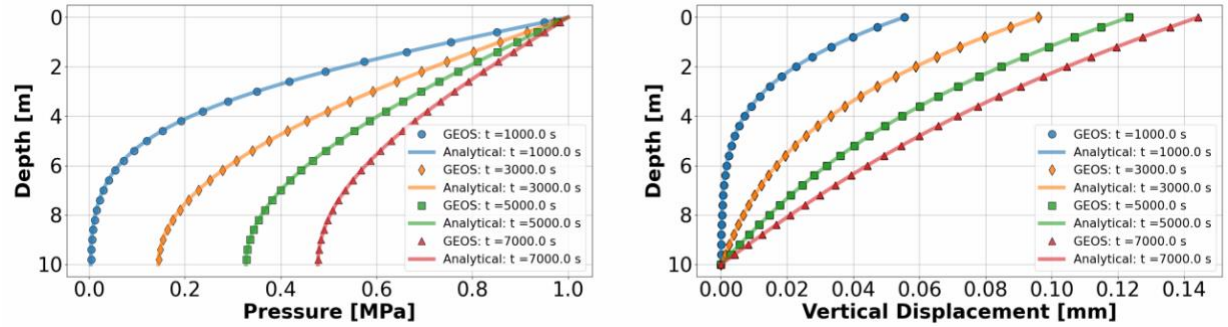

Fig.3 Comparisons between GEOS numerical results (marker) and analytical solutions (lines) for the 1D consolidation problem subject to fluid loading: (a) pore pressure; (b) vertical displacement.

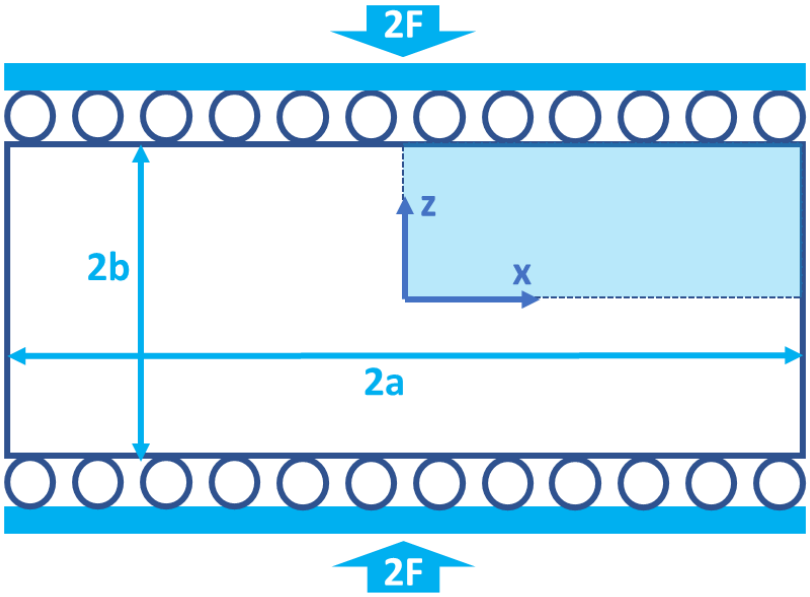

Fig.4 Sketch of the setup for Mandel's problem.

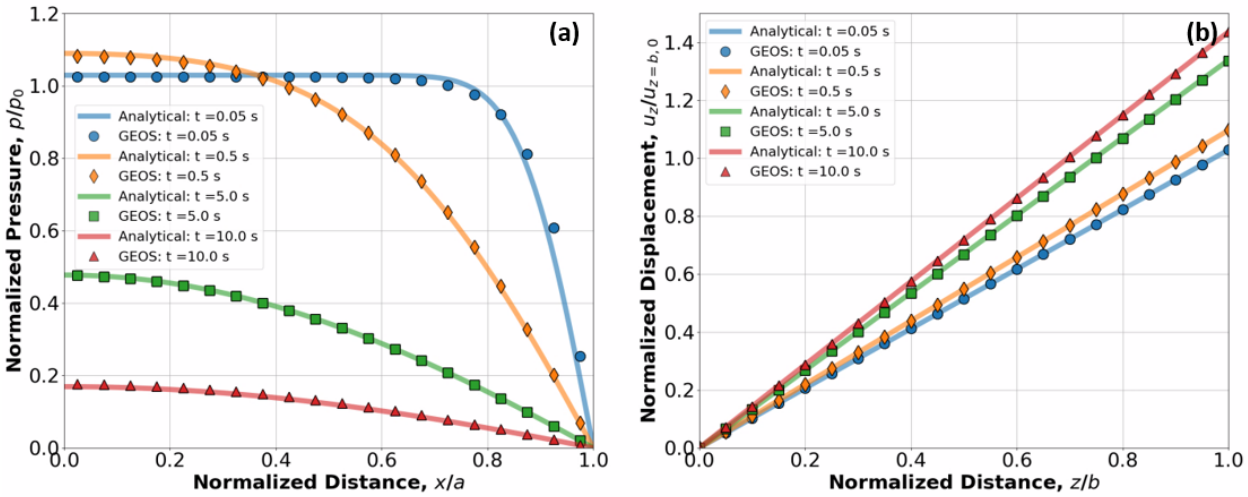

Fig.5 Comparisons between GEOS numerical results (marker) and analytical solutions (lines) for the evolution of (a) pore pressure along the x-axis; (b) vertical displacement along the z-axis.

Fig.6 Sketch of the setup for the Buckley-Leverett problem.

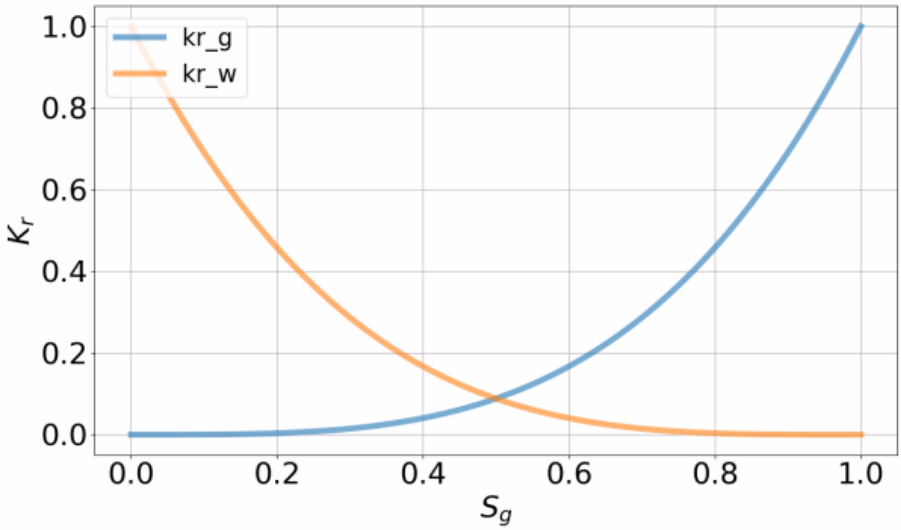

Fig.7 Relative permeabilities of two phases (CO2-rich phase and an aqueous phase).

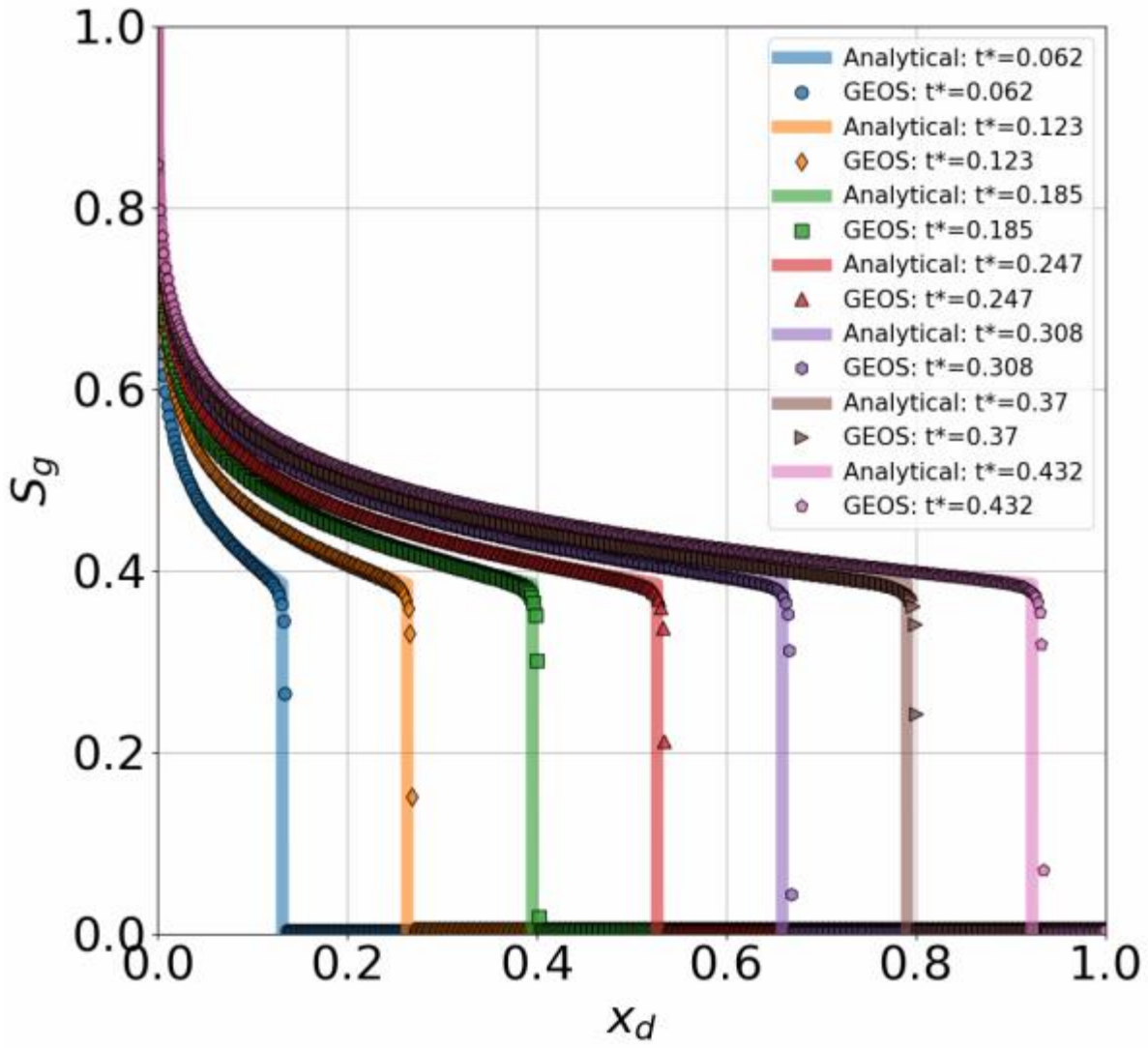

Fig.8 Comparison between GEOS numerical results (marker) and analytical solutions (lines) for the evolution of the non-wetting phase saturation along the flow direction.

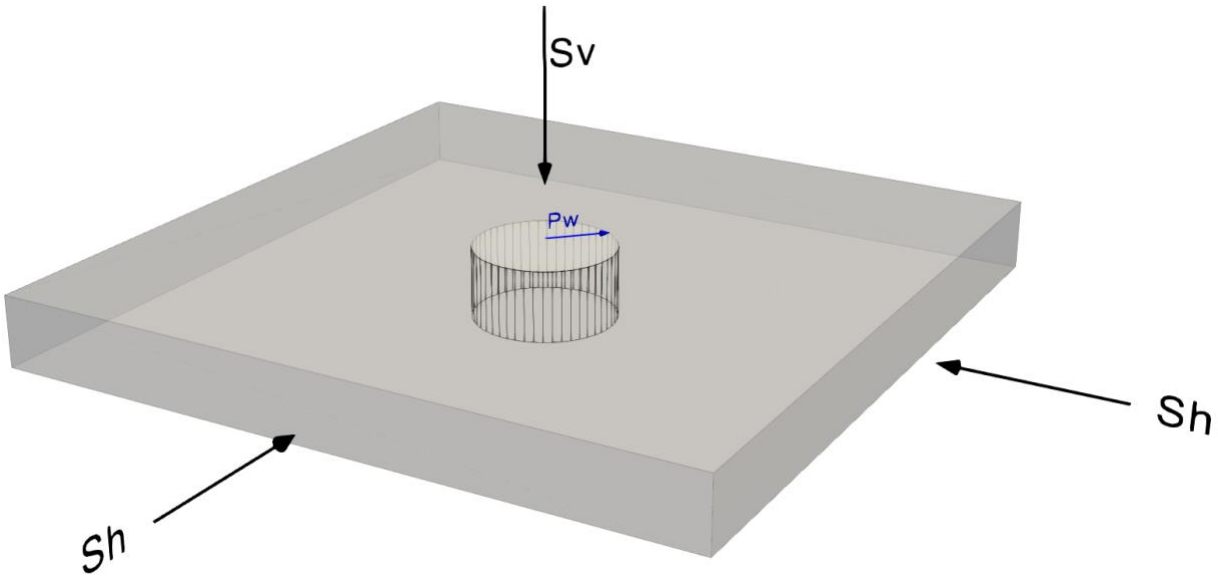

Fig.9 Sketch of the setup for a vertical wellbore problem.

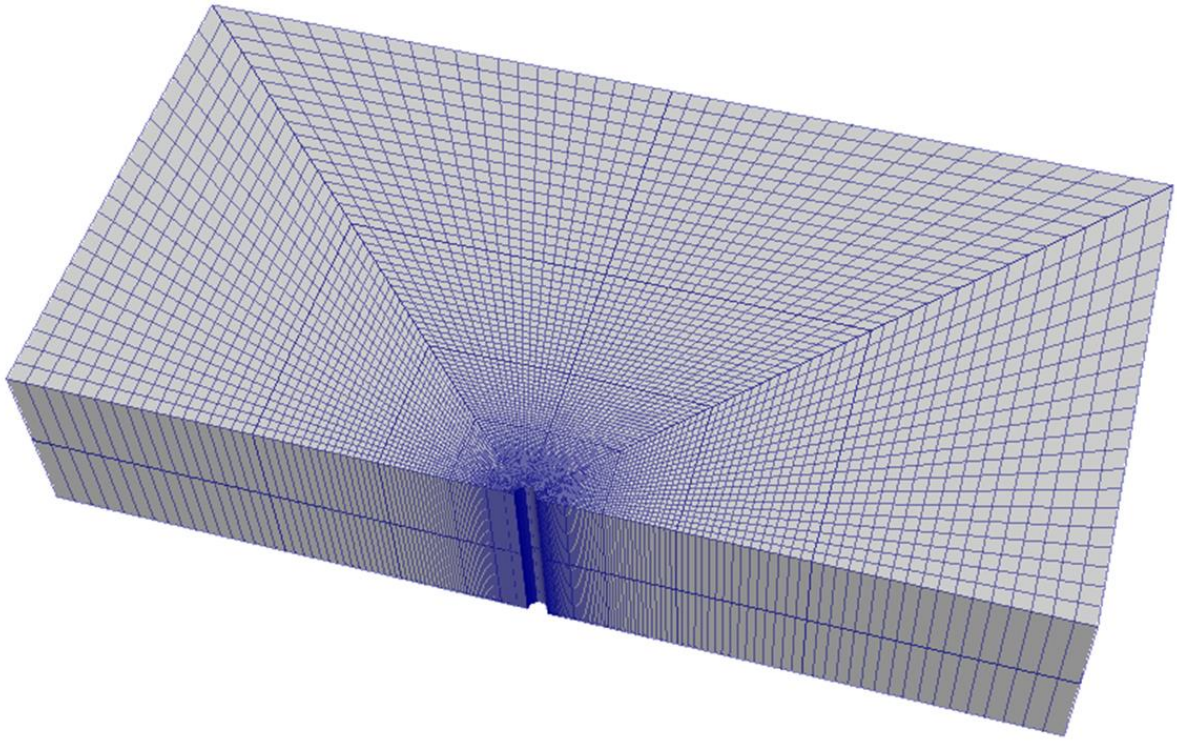

Fig.10 Mesh used for the vertical wellbore problem.

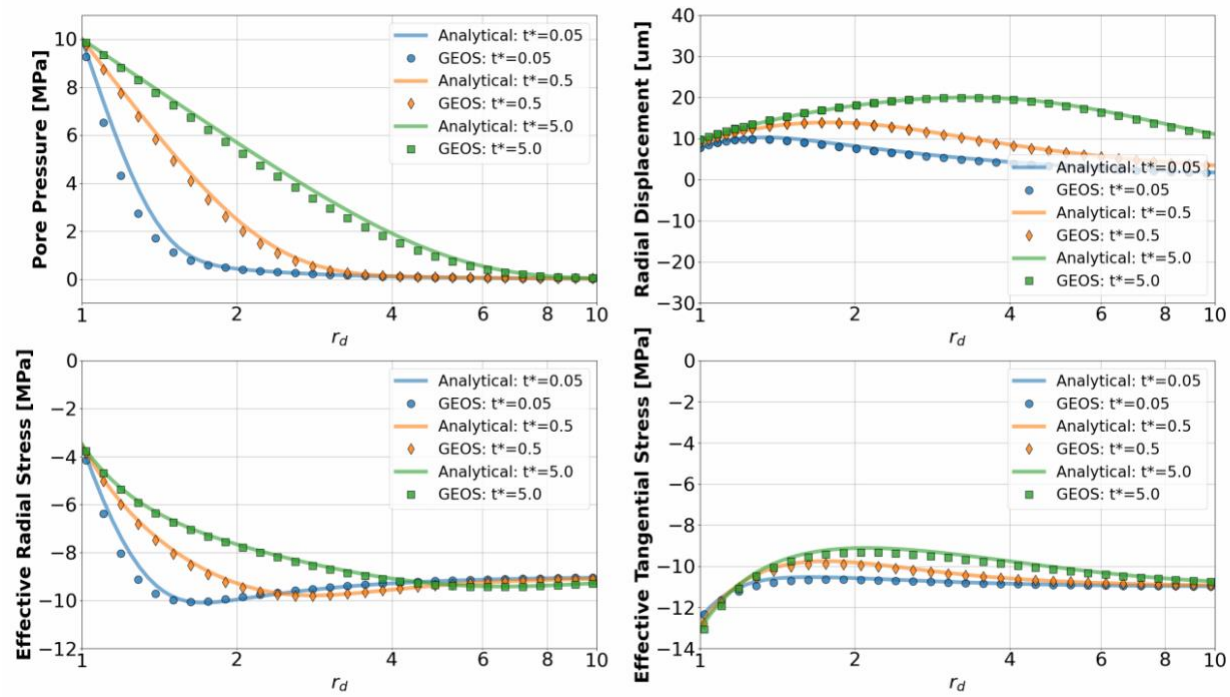

Fig.11 Comparisons between GEOS numerical results (marker) and analytical solutions (lines) for the evolution of (a) pore pressure, (b) radial displacement, (c) effective radial stress and (d) effective tangential stress along the σ_h direction.

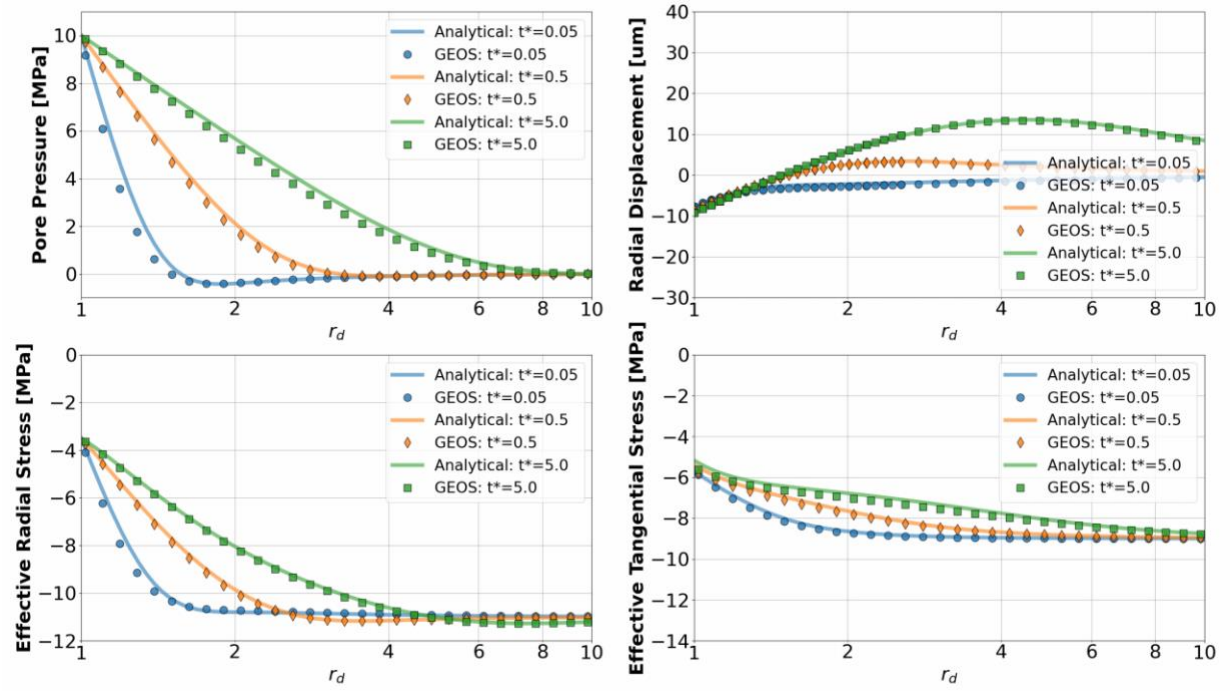

Fig.12 Comparison between GEOS numerical results (marker) and analytical solutions (lines) for the evolution of (a) pore pressure, (b) radial displacement, (c) effective radial stress and (d) effective tangential stress along the σ_H direction.

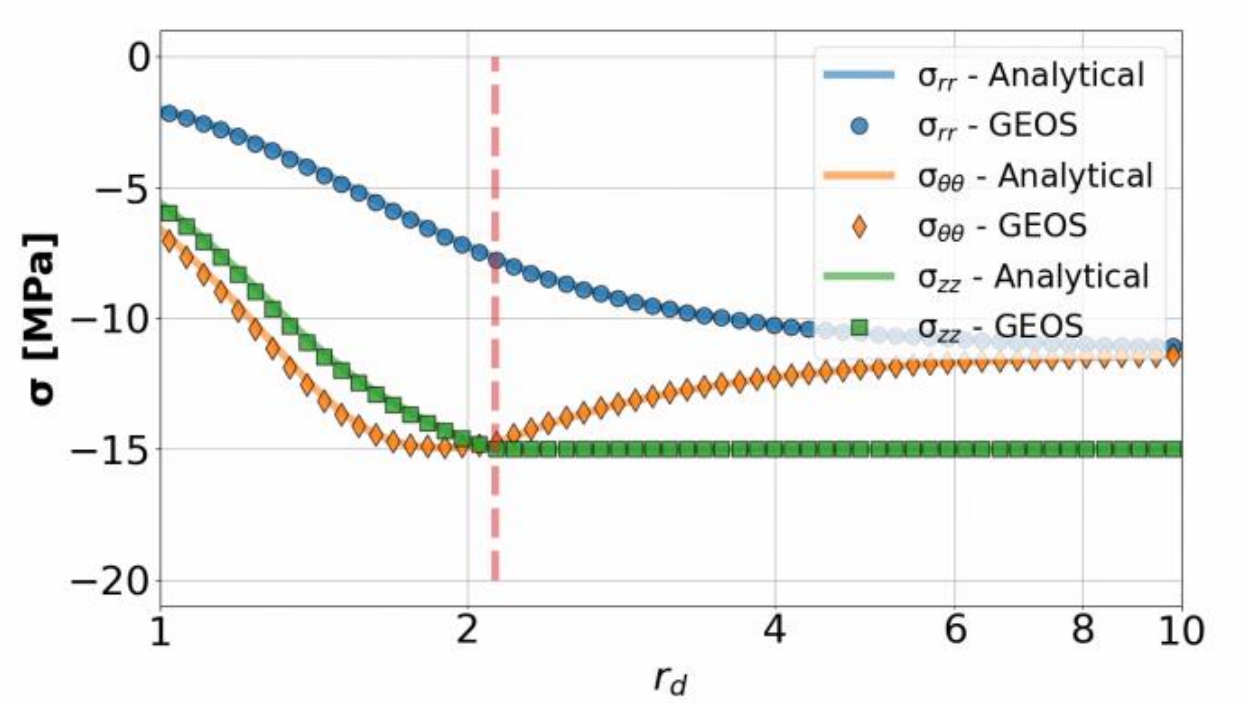

Fig.13 Comparison between GEOS numerical results (marker) and analytical solutions (lines) for the distribution of stress fields and location of elastic-plastic boundary (red dash line).

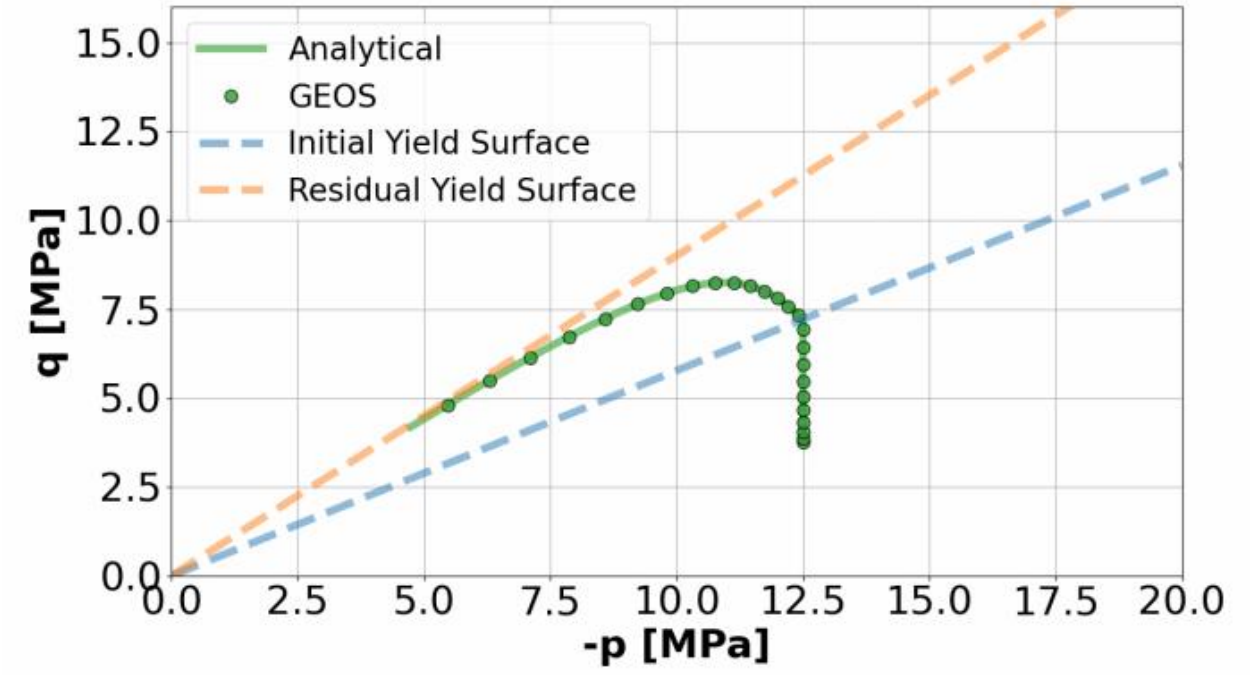

Fig.14 Comparison between GEOS numerical results (marker) and analytical solutions (lines) for stress path at the wellbore wall.

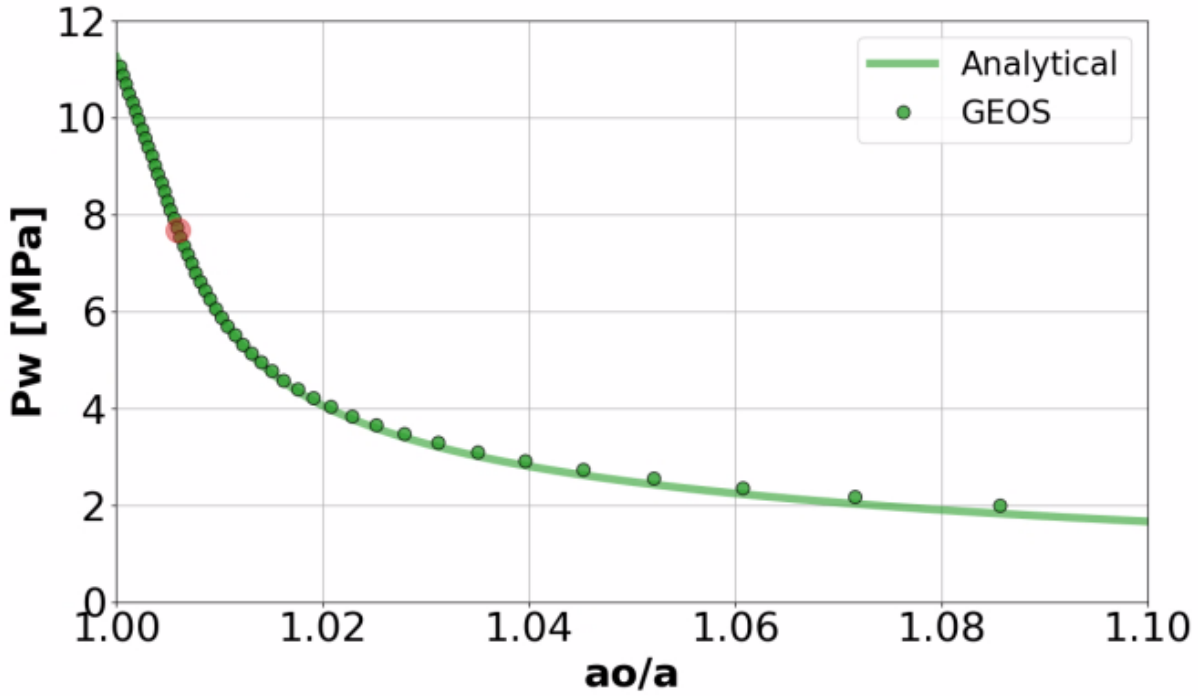

Fig.15 Comparison between GEOS numerical results (marker) and analytical solutions (lines) for normalized borehole radius under different wellbore support pressures.

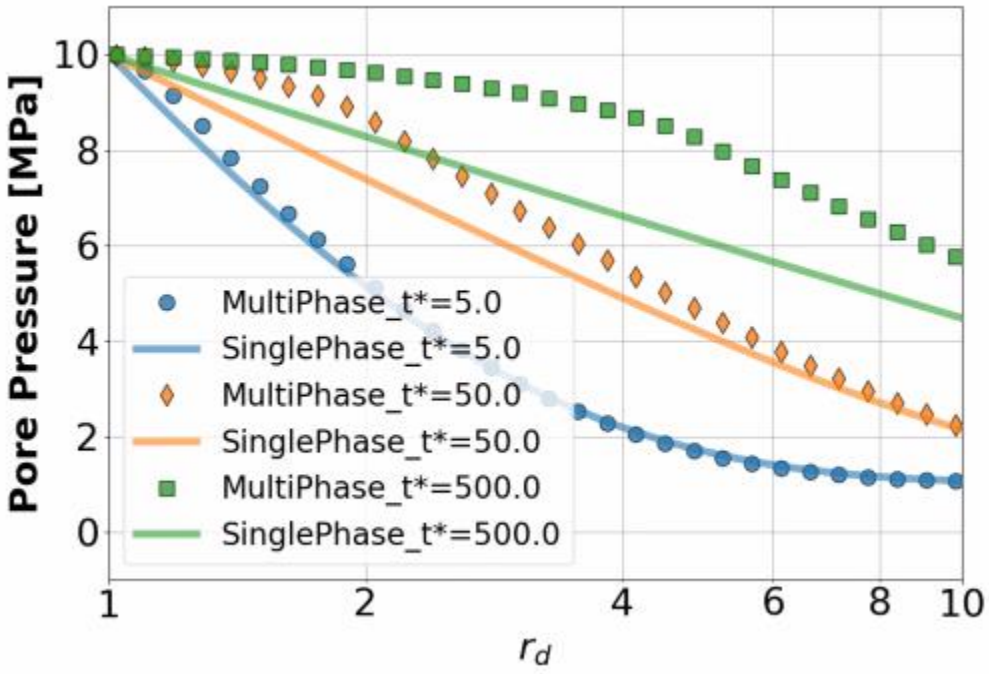

Fig.16 Comparisons between the poroelastic models with multiphase flow (marker) and single-phase flow (lines) for the distribution of pore pressure along the Radial distance at various times.

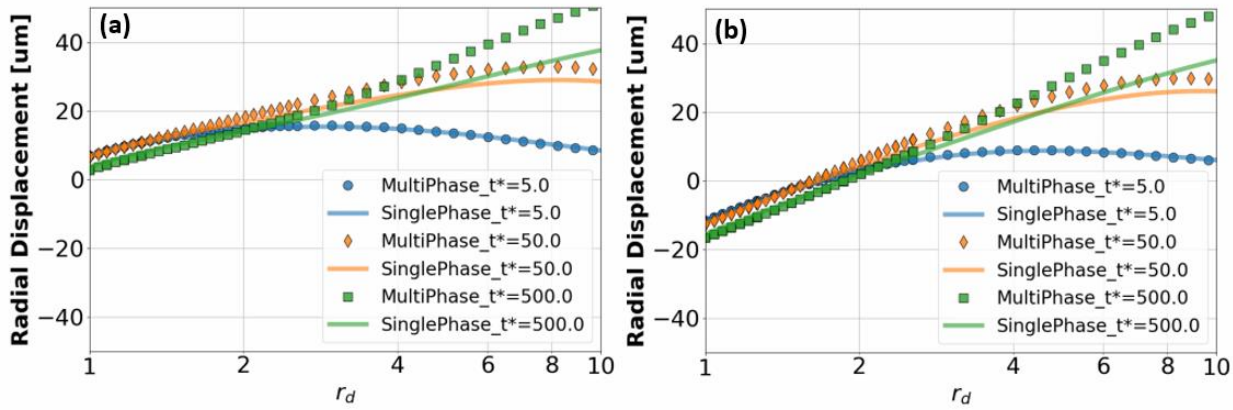

Fig.17 Comparisons between the poroelastic models with multiphase flow (marker) and single-phase flow (lines) for the distribution of induced radial displacements along: (a) σ_h direction; (b) σ_H direction.

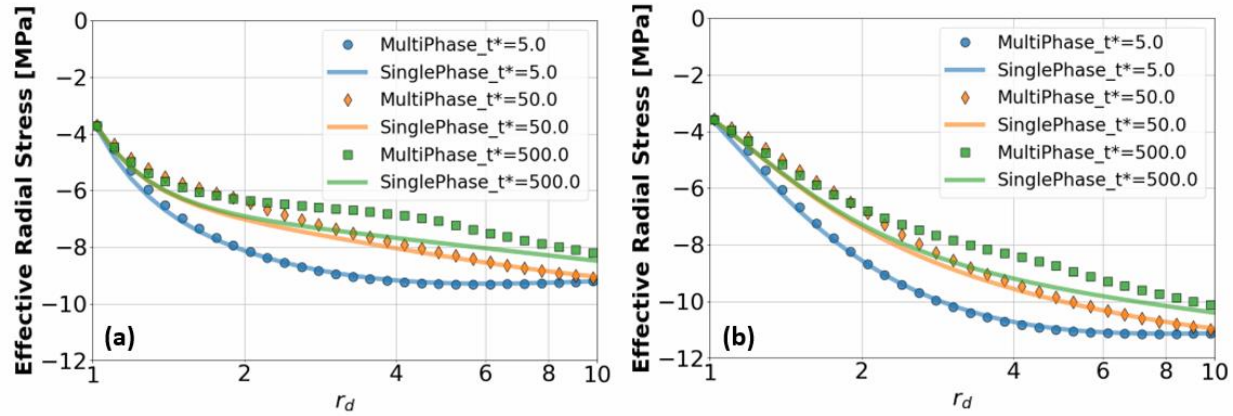

Fig.18 Comparisons between the poroelastic models with multiphase flow (marker) and single-phase flow (lines) for the distribution of effective radial stress along: (a) σ_h direction; (b) σ_H direction.

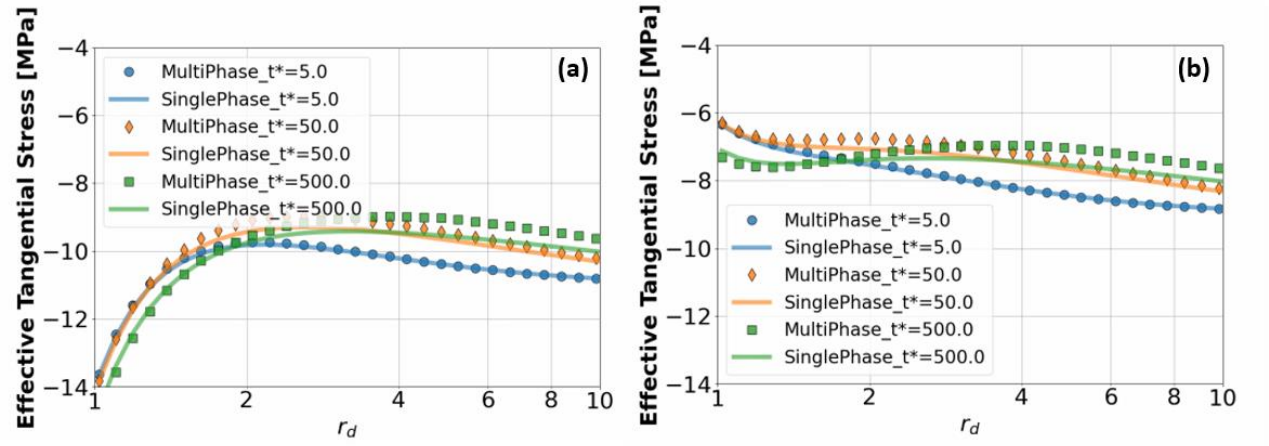

Fig.19 Comparisons between the poroelastic models with multiphase flow (marker) and single-phase flow (lines) for the distribution of effective tangential stress along: (a) σ_h direction; (b) σ_H direction.

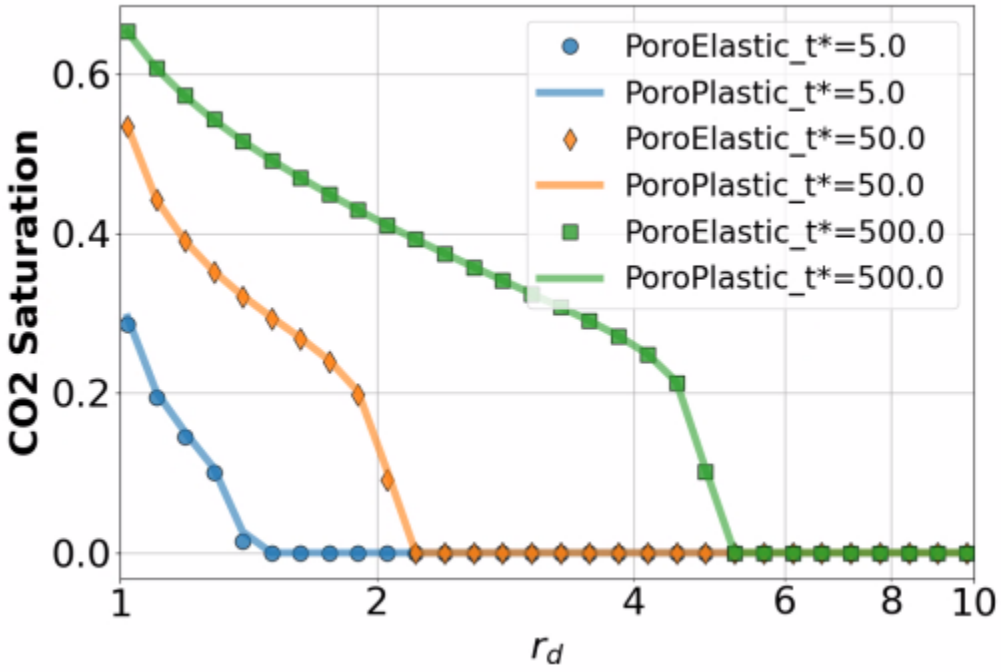

Fig.20 Comparisons between the poroelastic (marker) and the poroplastic (lines) models for the saturation of CO_2-rich phase along the radial distance at various times.

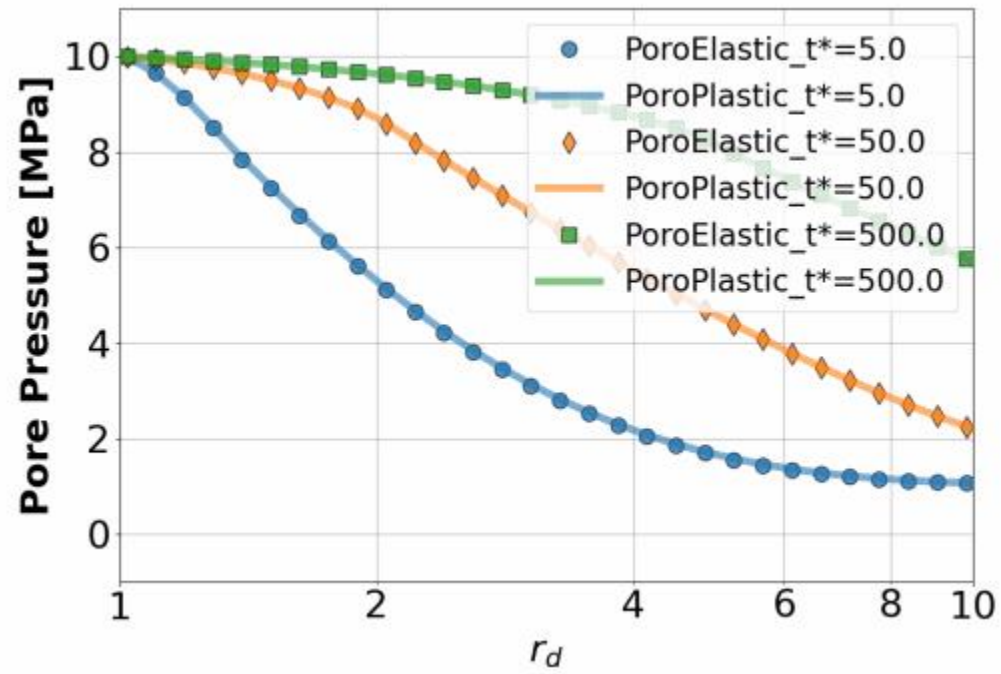

Fig.21 Comparisons between the poroelastic (marker) and the poroplastic (lines) models for the distribution of pore pressure along the Radial distance at various times.

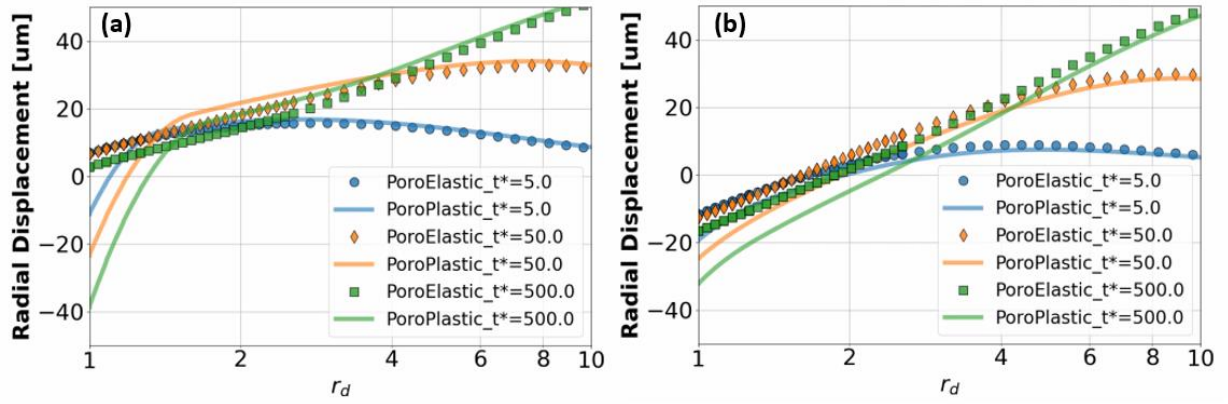

Fig.22 Comparisons between the poroelastic (marker) and the poroplastic (lines) models for the distribution of induced radial displacements along: (a) σ_h direction; (b) σ_H direction.

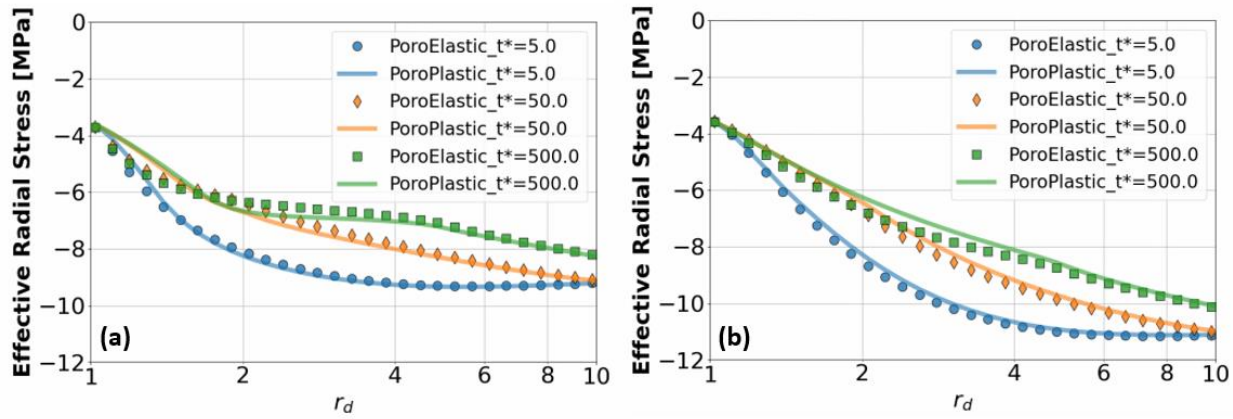

Fig.23 Comparisons between the poroelastic (marker) and the poroplastic (lines) models for the distribution of effective radial stress along: (a) σ_h direction; (b) σ_H direction.

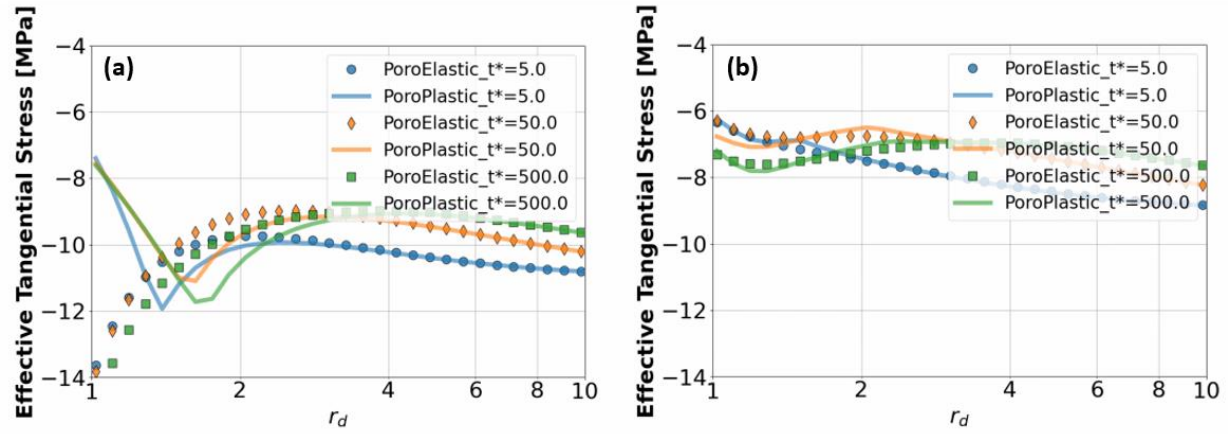

Fig.24 Comparisons between the poroelastic model (marker) and poroplastic (lines) for the distribution of effective tangential stress along: (a) σ_h direction; (b) σ_H direction.

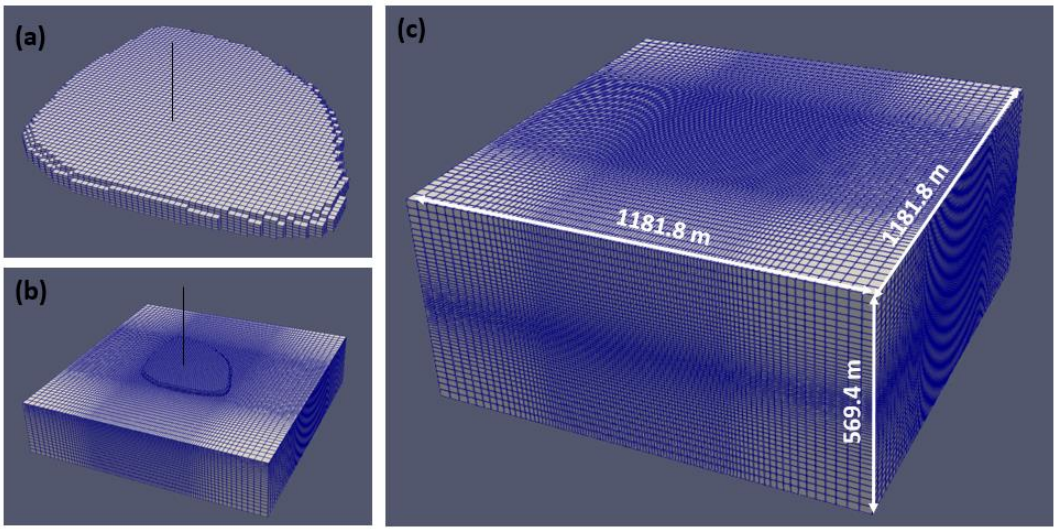

Fig.25 Reservoir geometry and used mesh for the Egg problem: (a) aquifer and injection well (black line); (b) aquifer, injection well (black line) and under burden; (c) entire domain.

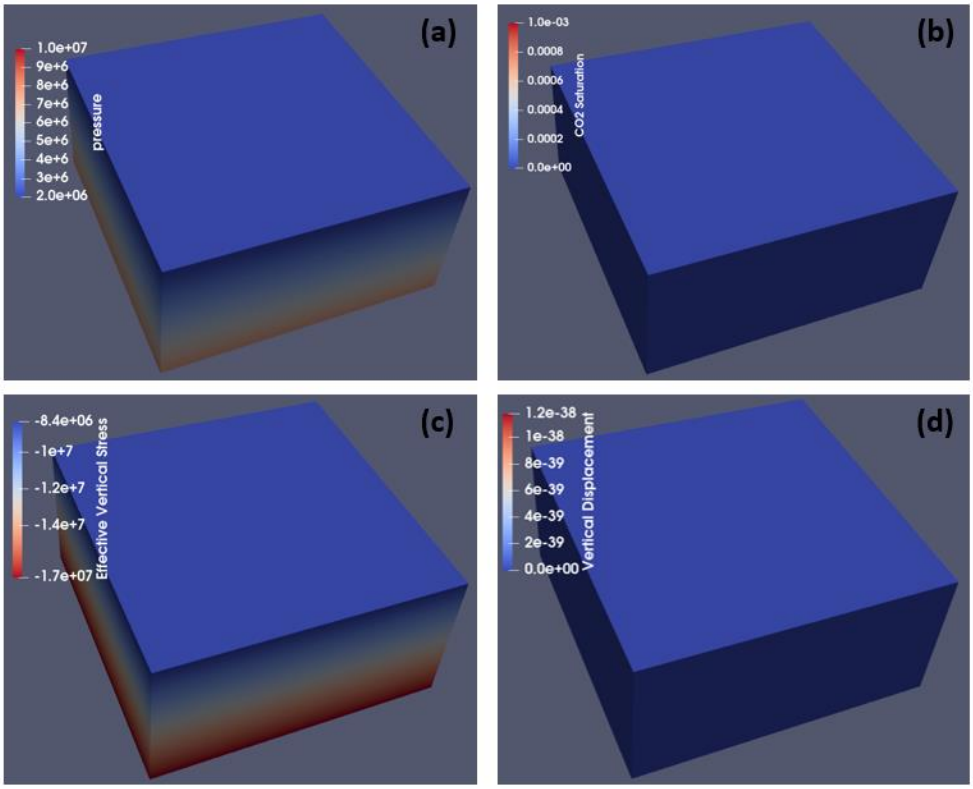

Fig.26 Initial conditions for the Egg problem: (a) pore pressure; (b) CO_2 saturation; (c) effective vertical stress; (d) vertical displacement.

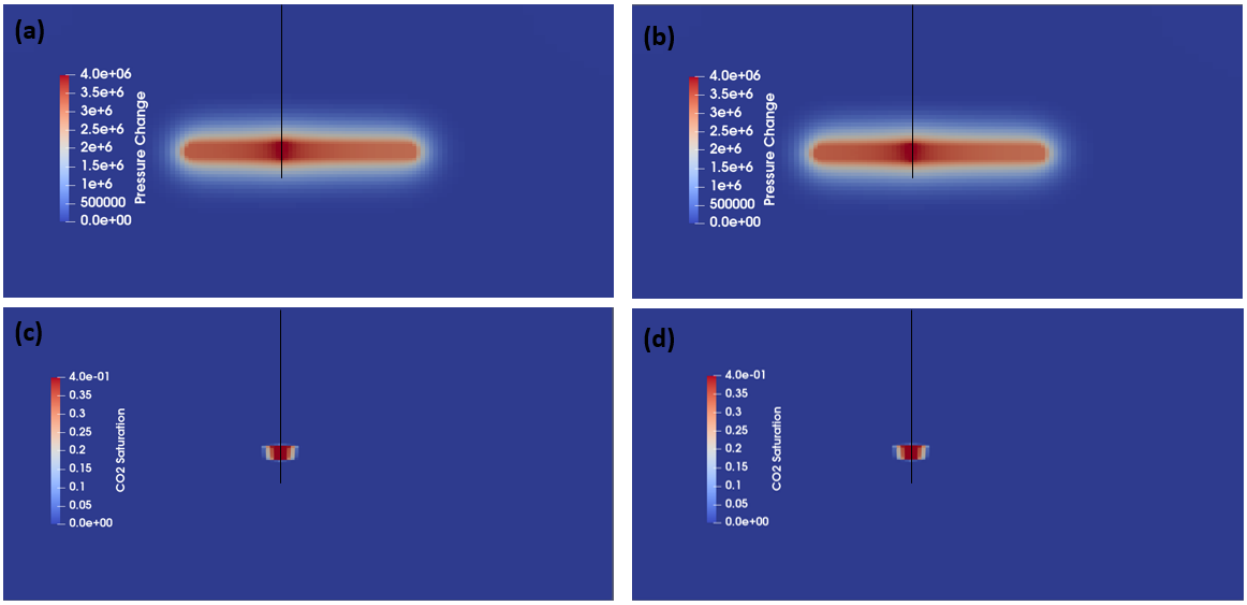

Fig.27 The location of injection well (black line) and cross section of the spatial distributions of pore pressure change ((a) poroelastic model and (b) poroplastic model) and CO_2 saturation ((c) poroelastic model and (d) poroplastic model) after 6-month injection.

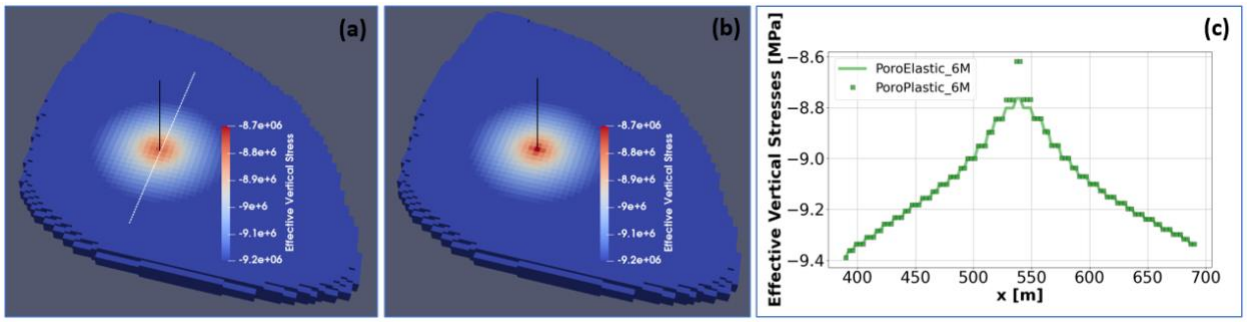

Fig.28 The location of injection well (black line) and the spatial distributions of effective vertical stress from (a) poroelastic model, (b) poroplastic model after 6-month injection. (c) Comparisons between poroplastic results (marker) and poroelastic solutions (lines) for the distribution of effective vertical stress along a horizontal line on top of the aquifer (white dashed line in (a)).

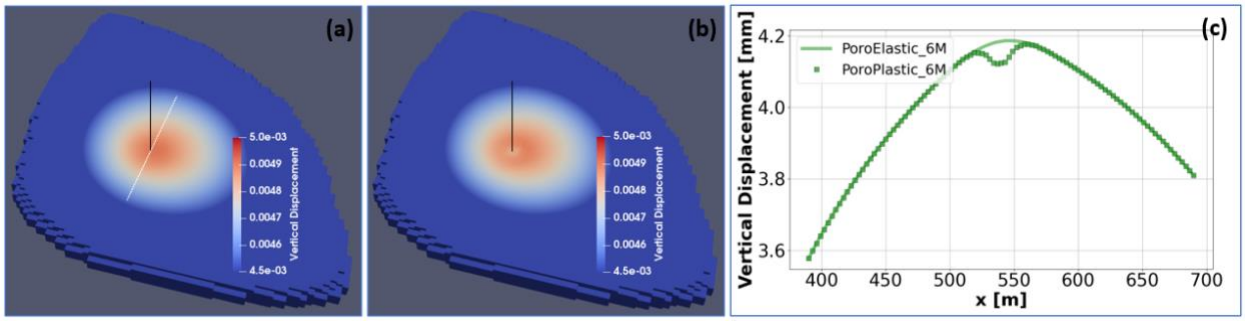

Fig.29 The location of injection well (black line) and the spatial distributions of vertical displacement from (a) poroelastic model, (b) poroplastic model after 6-month injection. (c) Comparisons between poroplastic results (marker) and poroelastic solutions (lines) for the distribution of vertical displacement along a horizontal line on top of the aquifer (white dashed line in (a)).